Catalysis Today 340 (2020) 70–85

Contents lists available at ScienceDirect

Catalysis Today

journal homepage: www.elsevier.com/locate/cattod

Solid-state synthesis, characterization, UV-induced coloration and photocatalytic activity – The $Sr_6Bi_2O_{11}$, $Sr_3Bi_2O_6$ and $Sr_2Bi_2O_5$ bismuthates

D.S. Shtarev[a,b], A.V. Shtareva[a], V.K. Ryabchuk[c], A.V. Rudakova[c], P.D. Murzin[c], M.S. Molokeev[b,d,e], A.V. Koroleva[c], A.I. Blokh[b], Nick Serpone[f,*]

[a] Yu. A. Kosygin Institute of Tectonics and Geophysics, Far Eastern branch of the Russian Academy of Sciences, 65 Kim Yu Chen Street, Khabarovsk, 680063, Russian Federation
[b] Far Eastern State Transport University, 47 Seryshev Street, Khabarovsk, 680021, Russian Federation
[c] St. Petersburg State University, Ulianovskaya 2, Petergof, Saint-Petersburg, 198904, Russian Federation
[d] Kirensky Institute of Physics, Akademgorodok 50, bld. 38, Krasnoyarsk, 660036, Russian Federation
[e] Siberian Federal University, 79 Svobodny pr., 660041, Krasnoyarsk, Russian Federation
[f] PhotoGreen Laboratory, Dipartimento di Chimica, Universita di Pavia, via Taramelli 12, Pavia, 27100, Italy

ARTICLE INFO

Keywords:
Photocatalysts
Strontium bismuthates
Photocatalytic activity
UV-induced coloration

ABSTRACT

This article reports on two novel strontium bismuthate photocatalysts ($Sr_6Bi_2O_{11}$ and $Sr_3Bi_2O_6$) prepared by a solid-state synthesis for which the number of strontium atoms exceeds the number of bismuth atoms in the cation sublattice; for comparison, the bismuthate $Sr_2Bi_2O_5$ was also re-examined. All three bismuthates were characterized by a variety of spectroscopic techniques (XRD, XPS, EDX, DR, Raman, SEM, and EIS). Direct bandgap energies for the three bismuthates were assessed from diffuse reflectance spectra: 2.61 eV for $Sr_6Bi_2O_{11}$; 3.40 eV for $Sr_3Bi_2O_6$; 3.17 eV for $Sr_2Bi_2O_5$, while the flatband potentials (versus NHE) of the corresponding valence bands were estimated from XPS spectra: +2.22 eV for $Sr_6Bi_2O_{11}$; +1.71 eV for $Sr_3Bi_2O_6$; +1.61 eV for $Sr_2Bi_2O_5$. The two novel bismuthates displayed photocatalytic activity toward the photodegradation of acetaldehyde in the gas phase and phenol in aqueous media, with the $Sr_6Bi_2O_{11}$ system exhibiting significantly greater photoactivity *vis-à-vis* the $Sr_3Bi_2O_6$ bismuthate; by comparison, $Sr_2Bi_2O_5$ was photocatalytically inactive in this case; their photoactivity was also assessed from the photodegradation of phenol in aqueous media (in all cases using UV-Vis irradiation from a Xe light source). Detailed photocatalytic mechanisms are proposed based on UV-induced coloration studies (carried out using a high-pressure Hg lamp; 365 nm) and on the photodegradation in the presence of radical scavengers to explain how composition and structure of the three bismuthates affect their photocatalytic activity. The role of point defects (oxygen vacancies) in their crystal lattice is described as they affect photocatalytic activity by acting as electron traps and potentially as electron/hole recombination centers.

1. Introduction

The search for new solid-state visible-light-active (VLA) photocatalytic materials has been one of the main streams in the field of Heterogeneous Photocatalysis in the last two decades [1,2]. Two basic approaches have been followed in producing VLA photocatalysts: (i) modification of well-known photocatalysts such as TiO_2 and ZnO (among others), by dye sensitization, by metal and nonmetal doping, by forming heterostructured composites involving either TiO_2 or ZnO that include Z schemes [3–5]; and (ii) search for innovative semiconductor materials that include complex metal-oxide and non-oxide solids together with their composites [6–10]. A group of different photoactive materials includes Bi-related photocatalysts and photocatalytic composites [1,11].

Bandgap energies (E_{bg}) of various bismuthate systems range from 2 to 3 eV, and as such, band-to-band photoexcitation involves a significant part of visible light radiation. For instance, bandgap energies are practically identical (2.5–2.7 eV) for the complex ternary metal oxides $Bi_4Ti_3O_{12}$, Bi_2WO_6, $BiVO_4$, and Bi_2MoO_6, decrease from 3.6 to 1.8 eV in BiOX (X = F, Cl, Br, I) systems, and change irregularly (range: 2.6–1.8 eV) for $MBiO_3$ (M = Li, K, Na, Ag) ternary systems. Flatband potentials of conduction (CB) and valence (VB) bands of many

* Corresponding author.
E-mail addresses: shtarev@mail.ru (D.S. Shtarev), avshtareva@mail.ru (A.V. Shtareva), v.ryabchuk@spbu.ru (V.K. Ryabchuk), arudakova@mail.ru (A.V. Rudakova), p.d.murzin@gmail.com (P.D. Murzin), msmolokeev@mail.ru (M.S. Molokeev), dalika@inbox.ru (A.V. Koroleva), blokh@rambler.ru (A.I. Blokh), nick.serpone@unipv.it (N. Serpone).

https://doi.org/10.1016/j.cattod.2018.09.035
Received 23 July 2018; Received in revised form 21 August 2018; Accepted 28 September 2018
Available online 13 October 2018
0920-5861/

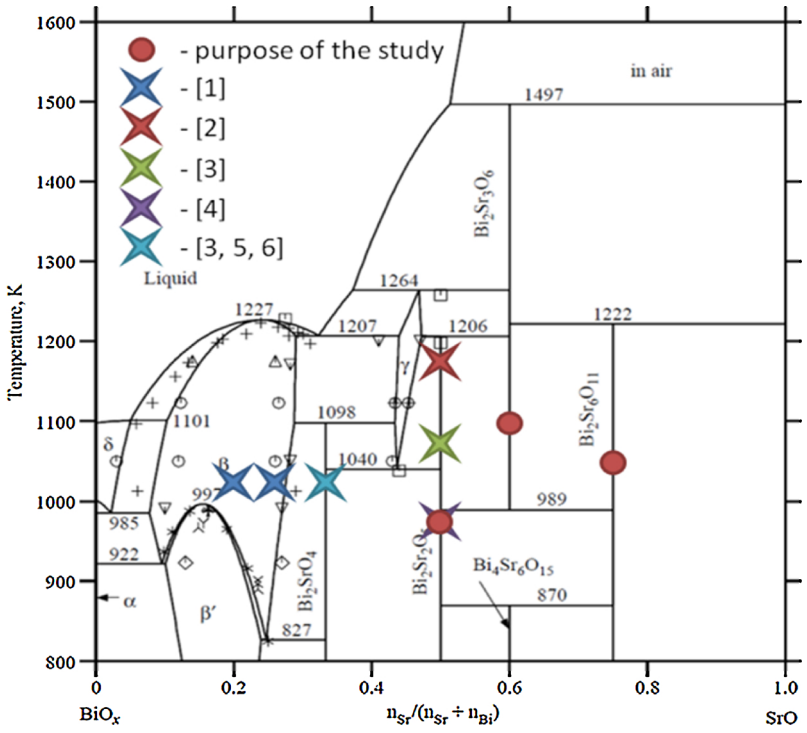

Fig. 1. Phase diagram of strontium bismuthates from B. Hallstedt, L. J. Gauckler, *Computer Coupling of Phase Diagrams and Thermochem.*, 27 (2003) 177–191 (ref. [24]). Colored markers represent the strontium bismuthates that are known photocatalysts. Red solid circles denote the bismuthates examined in this study.

bismuthates are favorable to carry out exothermic redox reactions ([11] and refs. therein). In fact, bandgap energies in the range $2.0 < E_{bg} < 3.0$ eV and flatband potentials of CB and VB bands, for what might be considered good photocatalysts, are exhibited by various Bi-based compounds of different chemical compositions, crystalline structures and physicochemical properties. Consequently, a search for novel Bi-based photocatalysts that might possess such attributes is worth carrying out. In this regard, bismuthates are, *a priori*, promising candidates in photocatalysis, particularly the calcium [12–16] and strontium [17–22] bismuthates.

Within this context, this article reports the solid-state synthesis of $Sr_2Bi_2O_5$, $Sr_3Bi_2O_6$, and $Sr_6Bi_2O_{11}$, the latter two being novel materials, together with a concomitant investigation into their optical, structural, and photocatalytic properties. Germane to the present study, Shtarev and coworkers [23] reported that the potential of the bottommost energy level of the conduction band of strontium bismuthates depends on the ratio of the number of strontium to bismuth atoms in the cation sublattice. The most promising compositions are those in which the number of strontium atoms in the cationic sublattices equals or exceeds the number of bismuth atoms. Judging from the phase diagram of Fig. 1 [24], such compositions include the strontium bismuthates $Sr_2Bi_2O_5$, $Sr_3Bi_2O_6$, and $Sr_6Bi_2O_{11}$; the photocatalytic properties of $Sr_2Bi_2O_5$ were reported earlier [19, 20] but are revisited herein for comparison with the two new bismuthates. To the best of our knowledge, the nature and photocatalytic properties of the two ternary systems $Sr_3Bi_2O_6$ and $Sr_6Bi_2O_{11}$ have not heretofore been reported nor investigated.

2. Experimental

2.1. Synthesis of the strontium bismuthates

Perusal of the phase diagram of Fig. 1 (red solid circles) reveals that the expected strontium bismuthate phases $Sr_2Bi_2O_5$, $Sr_3Bi_2O_6$ and $Sr_6Bi_2O_{11}$ correspond to a SrO content of 50, 60 and 75 at.%, respectively, in the cation sublattice. These polycrystalline strontium bismuthates were prepared by thorough mixing the two solids $Sr(NO_3)_2$ (≥99.5% purity; ACROS Chemicals) and Bi_2O_3 (≥99.5% purity; ACROS Chemicals) in stoichiometric proportions in an agate mortar for 40 min in the presence of absolute ethanol (puriss. grade, ≥99.8% (GC), Vekton). The mixtures were subsequently subjected to a two-stage heating procedure. In the first stage (heating at 650 °C for 24 hrs in air), strontium nitrate was converted to strontium oxide, whereas in the second stage they were heated at temperatures ≥700 °C for 72 h in air that ultimately yielded the three strontium bismuthates. Table 1 summarizes detailed conditions of the synthesis for each of the three bismuthates.

The as-prepared strontium bismuthate samples of different composition displayed different colors: yellow for $Sr_2Bi_2O_5$, beige for $Sr_3Bi_2O_6$, and khaki for $Sr_6Bi_2O_{11}$ as illustrated in **Figure S1** (Supplementary Information).

2.2. Material characterization

X-Ray Diffraction (XRD) analyses to assess which strontium bismuthate phase formed in the solid-state syntheses were performed employing a Rigaku Ultima IV diffractometer (Japan) with CuKα radiation (λ = 1.5406 Å) in the range $10 \leq 2\theta \leq 80$ degrees at a scanning speed of 2 deg. min^{-1}. Structural data of the strontium bismuthate phases were obtained from the PDF-2 database with phase identification carried out with the « Search Match! » software package [25].

The morphologies of the samples were determined by scanning

Table 1
Synthesis conditions in the preparation of the strontium bismuthates.

Expected strontium bismuthate phase (SrO content, %)	Content of starting materials, (mols)		Synthesis temperature, (°C)	
	$Sr(NO_3)_2$	Bi_2O_3	1st stage (24 hrs)	2nd stage (72 hrs)
$Sr_2Bi_2O_5$ (50)	1.50	0.75	650	700
$Sr_3Bi_2O_6$ (60)	1.50	0.50	650	825
$Sr_6Bi_2O_{11}$ (75)	1.50	0.25	650	775

electron microscopy (SEM; TESCAN, Czech Republic; acceleration voltage, 20 kV). The distribution and mapping of the elements in the bismuthate solids were established by Energy Dispersive X-Ray Spectroscopy (EDX; X-Max^N, Oxford Instruments, UK).

Raman spectra were recorded in the 80–1500 cm^{-1} spectral region at ambient temperature using the SENTERRA Raman spectrometer (Bruker; resolution, 2 cm^{-1}; laser excitation wavelength, 785 nm; laser beam power, 1 mW).

The specific surface area of the strontium bismuthates, pretreated at 350 °C for 6 hrs, was determined by the BET method using the Quadrasorb SI surface area analyzer.

Electrochemical impedance spectroscopy (EIS) was employed to examine the electrophysical properties of the as-synthesized samples as a further characterization tool. The NOVOCONTROL BDS dielectric spectrometer provided precision measurements of the complex conductivity over a wide frequency range (0.01 Hz to 40 MHz) and temperature (−100 °C to + 300 °C). The powdered samples were pressed into self-supported pellets (diameter, 8.9 mm; thickness, 1.2 mm) – results are reported in the Supplementary Information section.

Elemental compositions and valence band positions were determined from X-ray photoelectron spectra (XPS) recorded on a Thermo Fisher Scientific Escalab 250Xi spectrometer (Al Kα radiation, 1486.6 eV; spectral resolution, 0.5 eV); the reference carbon line C_{1s} (C—C bond) was seen at a binding energy (BE) of 284.8 eV [26].

Diffuse reflectance spectra, as R(λ), were recorded in the 250–1200 nm spectral range under ambient conditions on a Cary 5000 UV/vis/NIR spectrophotometer equipped with a DRA 2500 external diffuse reflectance accessory; optical-grade $BaSO_4$ was the reference standard. To investigate the UV-induced coloration, the solid samples were placed in home-made aluminum sample holders (diameter,15 mm; depth, 3 mm) covered with a quartz window, followed by irradiation in the spectral region 250–400 nm with a 120-W High-pressure Hg lamp (DRK-120; MELZ, Russia) and a UFS-2 bandpass filter (LOMO, Russia). Most of the light irradiance (15 mW cm^{-2}; NOVA 2 radiometer) in the spectral region 250–400 nm originated from the 365-nm mercury line.

2.3. Photocatalytic activity of the three strontium bismuthates

2.3.1. Gas-phase photocatalytic test – photodegradation of acetaldehyde in the gas phase

The photocatalytic activities of the as-synthesized bismuthates were evaluated in the gas phase using the decomposition of acetaldehyde as the test process by exposing the bismuthate solid/CH_3CHO mixtures to UV irradiation under otherwise identical irradiation conditions for comparison purposes. The ISO 22197-2 standard *Test method for air-purification performance of semiconducting photocatalytic materials, removal of acetaldehyde* [27] was used to assess the photoactivity of the bismuthates. The solids were pressed into self-supported pellets (46 mm × 70 mm size and 0.5 mm thick), placed into a special compartment, and then were pre-activated at 150 °C for 16 hrs after which they were placed in the flow-type reactor. The total gas flow rate was 0.18 L min^{-1} (ISO normal conditions); the concentration of acetaldehyde and moisture content in the gas flow was 5 ppm (i.e., a volume fraction of 5 μL L^{-1}) and 50%, respectively. The initial concentration of acetaldehyde in the CH_3CHO/N_2 gas mixture (Linde Gas Rus, JSC) was 1536 ppm.

Initial (before irradiation) and operating (during and after irradiation) concentrations of acetaldehyde in the flow were determined by GC analysis in a Model 8610C gas chromatograph with flame ionization detector (SRI Instruments); pre-irradiation and irradiation periods were 1 hr and 2 hrs, respectively. The light source was a 150-W Xe lamp (OSRAM); a cutoff optical filter ascertained the removal of UV wavelengths below 300 nm (light irradiance, 3 mW cm^{-2}).

According to the ISO test procedure, the photocatalytic activity (r) is taken as the relative change of the acetaldehyde concentration (in μmols) during the last hour of irradiation ($C_{h\nu}$) *versus* the concentration at the termination of the reaction (C_{dark}) as expressed by Eq. (1):

$$r = \frac{C_{h\nu} - C_{dark}}{C_{dark}} \bullet f \bullet C_{dark} \bullet \frac{1.016 \bullet 60}{22.4} \quad (1)$$

where $C_{h\nu}$ is the average volume fraction of acetaldehyde (μL L^{-1}) during the last hour of the photodegradation reaction; C_{dark} denotes the average volume fraction of acetaldehyde (μL L^{-1}) in the dark after termination of the photodegradation reaction; and f is the flow rate (L min^{-1}; ISO normal conditions).

2.3.2. Liquid-phase photocatalytic test – photodegradation of phenol in aqueous media

The photocatalytic activity of the bismuthates was also assessed in the liquid phase by the decomposition of phenol in a batch-type reactor with lateral quartz window; the photoreactor was subjected to UV irradiation under ambient conditions. Prior to irradiation, aqueous suspensions of the bismuthates (1.0 g L^{-1}; pH, 7.0; 300 mL) were pretreated in an ultrasonic processor for 10 min, followed by addition of phenol (100 ppm; purity, 99.5% Aldrich) to the suspensions and then magnetically stirred for 1 hr in the dark to achieve adsorption/desorption equilibria. The initial concentration of phenol was such that the photoreaction kinetics were independent of concentration. The light source was a 150-W Xe lamp (OSRAM); an optical cutoff filter ascertained the removal of UV wavelengths below 300 nm (light irradiance, 7 mW cm^{-2}). Evonik's P25 TiO_2 was also examined as the photocatalyst for comparison with the bismuthates simply to explore how they would compare with the most often used metal oxide in photocatalysis under otherwise identical conditions used for the bismuthates (e.g., the concentration ratio between photocatalyst and the phenol, concentration of phenol, UV–Vis irradiation, etc.).

Aliquot samples were collected at given intervals and filtered through a 0.2 μm Minisart filter to remove solid particles prior to HPLC analysis to determine the phenol concentration on a 1260 Infinity liquid chromatograph equipped with a UV–Vis detector and a C18 column (Agilent Technologies). The mobile phase was a 50/50 v/v mixture of methanol/water; detection wavelength was 210 nm at a bandwidth of 4 nm. The photocatalytic activity of the samples was estimated by the rate of photodegradation of phenol using the kinetic expressions (Eqs. (2) and (3)):

$$C(t) = C_0 \bullet exp(-kt) \quad (2)$$

$$dC/dC_{(t\rightarrow 0)} = -kC_0 \quad (3)$$

where k is a quasi-first-order rate constant.

To elucidate the mechanistic stages of the phenol photodegradation reaction, we examined the effect of selected radical scavengers on the reaction kinetics; the scavengers chosen were isopropanol (IPA; > 99.9% HPLC grade; Panreac) as the hydroxyl radical ($^{\bullet}OH$) scavenger, p-benzoquinone (p-BQ, > 98%, Sigma-Aldrich) as the superoxide radical anion ($O_2^{-\bullet}$) scavenger, and ammonium oxalate (AO, synthesized from oxalic acid and ammonium hydroxide) as the scavenger of photoholes (h^+). Initial phenol concentration and catalyst loading were, respectively, 100 ppm and 1.0 g L^{-1}. The concentration of the radical scavengers was in all cases 0.20 mM [28]; light irradiance for these experiments was 1 mW cm^{-2}.

In the presence of scavengers, the photocatalytic activity (A) of the bismuthates was estimated as the relative change of phenol concentration during the reaction period according to the expression of Eq. (4):

$$A = (C_0 - C_{8.5})/C_0 \quad (4)$$

where C_0 is the initial phenol concentration (ppm) and $C_{8.5}$ denotes the phenol concentration (ppm) after a reaction time of 8.5 hrs.

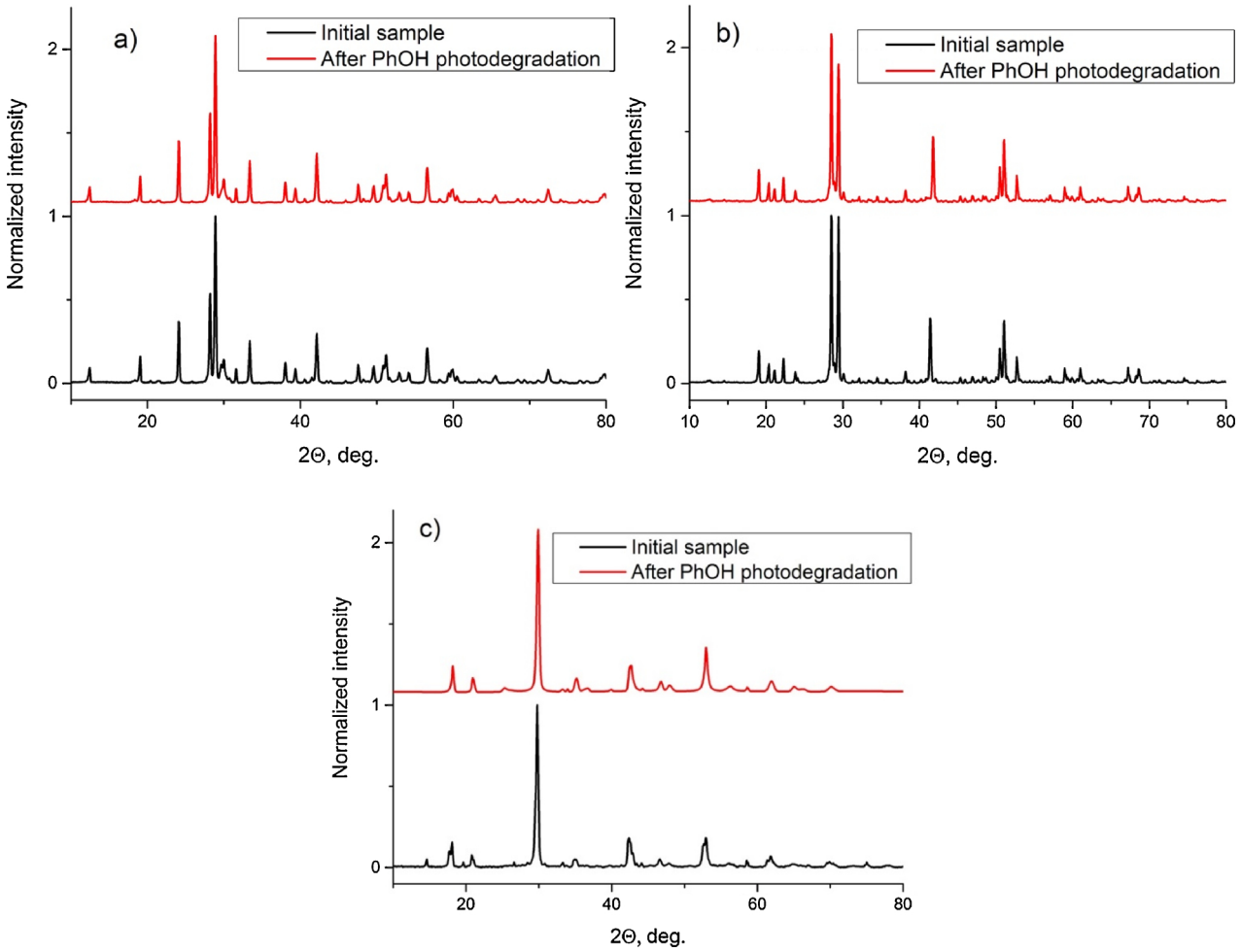

Fig. 2. XRD spectra of the as-synthesized bismuthates $Sr_2Bi_2O_5$, $Sr_3Bi_2O_6$ and $Sr_6Bi_2O_{11}$ before and after the photodegradation of phenol in aqueous media; note the bismuthates retain their full integrity after being subjected to the photocatalytic process.

3. Results

3.1. XRD, SEM and EDX characterization

XRD patterns of the three bismuthates illustrated in **Figure S2** demonstrate that the samples correspond to the $Sr_2Bi_2O_5$, $Sr_3Bi_2O_6$, and $Sr_6Bi_2O_{11}$ phases [29–31]. The synthesis conditions summarized in Table 1 were appropriate in producing highly crystalline strontium bismuthates with a SrO content ≥ 50 at.% in the cation sublattice. Fig. 2 displays the XRD spectra of the bismuthates $Sr_2Bi_2O_5$, $Sr_3Bi_2O_6$ and $Sr_6Bi_2O_{11}$ recorded before and after the photodegradation of phenol in aqueous media to examine their structural integrity; clearly the bismuthates retain their full integrity after being subjected to the photocatalytic process.

Cell parameters of the as-prepared samples are listed in Table 2. The strontium bismuthate samples pretreated at 350 °C for 6 hrs possessed comparable and relatively small specific surface areas (Table 2), typically observed for compounds synthesized by solid-state reactions. Consequently, the photocatalytic activities of the bismuthates used in the photocatalytic tests can be compared with the proviso that the same quantities of the bismuthate solids are used.

The as-synthesized strontium bismuthates adopt a crystal lattice of the «coordinate + graded» translational type. The $Sr_2Bi_2O_5$ bismuthate possesses the crystal lattice of the non-symmetric base-centered orthorhombic space group *Cmcm* belonging to the lower symmetry class *mmm*, while $Sr_3Bi_2O_6$ adopts the crystal lattice of the symmorphic space group that belongs to the middle class *3 m* syngony; the $Sr_6Bi_2O_{11}$ bismuthate also adopts the crystal lattice of a symmorphic space group (*I4/mmm*). The pertinent space group diagrams of the three bismuthates are reported in **Figure S3**, which reveals that the $Sr_2Bi_2O_5$ and $Sr_6Bi_2O_{11}$ systems are characterized by similar atom packing in the crystal lattice, as well as the orientation of the crystal lattice in space, whereas the $Sr_3Bi_2O_6$ is significantly different. This explains why the unit cell volume of $Sr_3Bi_2O_6$ is nearly eightfold greater than those of $Sr_2Bi_2O_5$ and $Sr_6Bi_2O_{11}$.

Fig. 3 presents the scanning electron microscopy (SEM) images of the strontium bismuthates and reveals that the particles composition defines not only their crystal structures but also some peculiarities of

Table 2
Cell parameters and specific surface area of the as-prepared strontium bismuthates.

Parameters	Sample		
Phase	**$Sr_2Bi_2O_5$**	**$Sr_3Bi_2O_6$**	**$Sr_6Bi_2O_{11}$**
Crystal lattice	Base-centered orthorhombic	Rhombohedrally-centered trigonal	body-centered tetragonal
Space group	*Cmcm*	*R* 3 *m*	*I4/mmm*
Cell parameters:			
a, Å	3.8261	12.526	6.0058(3)
b, Å	14.3066	–	–
c, Å	6.1715	18.331	8.3718(5)
Cell volume, Å^3	337.82	2490.82	301.97
S_{BET}, m^2 g^{-1}	0.72	1.11	0.74

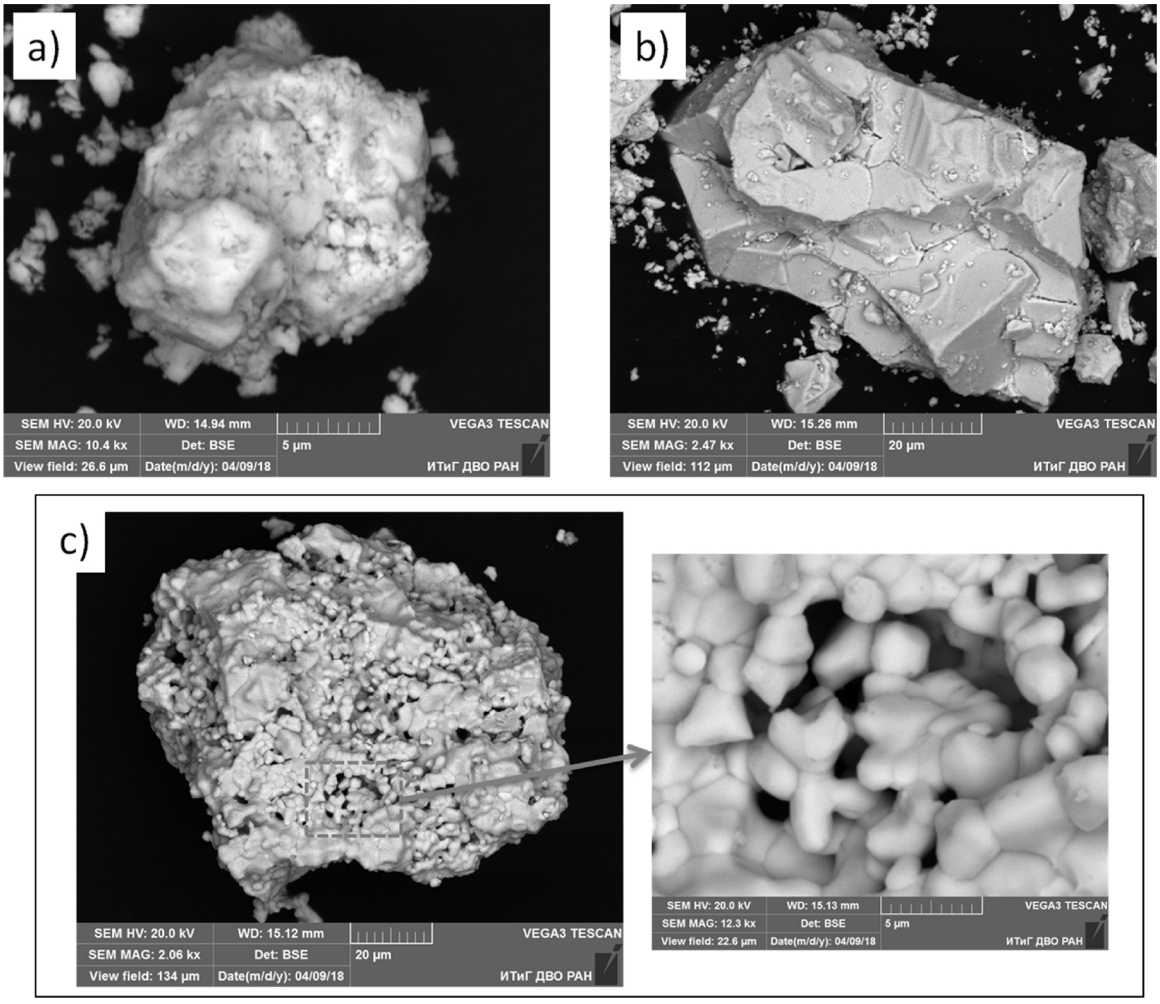

Fig. 3. SEM images of strontium bismuthate synthesized particles (a) $Sr_2Bi_2O_5$, (b) $Sr_6Bi_2O_{11}$, and (c) $Sr_3Bi_2O_6$.

the surface morphology. For example, particles of the $Sr_2Bi_2O_5$ and $Sr_6Bi_2O_{11}$ phases (Fig. 3a and b) display similar features: namely, the sizes of the particles are several tens of micrometers with no visible pores or other features that might increase the specific surface area. Although the $Sr_3Bi_2O_6$ particles are of similar sizes (several tens of micrometers), they reveal voids and pores on the surface (Fig. 3c) that explain the slightly greater specific surface area in comparison to the other two bismuthates.

The EDX spectra of the as-synthesized bismuthates are shown in **Figures S4–S6**, and report the measured strontium-to-bismuth ratios that parallel the stoichiometric composition of the samples; Sr/Bi ratios are 0.94 (13.0 at.% ÷ 13.8 at.%) for $Sr_2Bi_2O_5$, 1.42 for $Sr_3Bi_2O_6$, and 2.82 for the $Sr_6Bi_2O_{11}$ bismuthate.

3.2. Raman spectral analysis

Raman spectra of the three bismuthates are illustrated in Fig. 4; germane to these, the Raman spectrum of Bi_2O_3 reported by Betsch and White [32] and by Narang and coworkers [33] indicates that bismuth does not adopt a simple structure; rather, new phases containing bismuth are formed such as, for instance, pyramidal BiO_3 and octahedral BiO_6 units. Raman spectral bands of bismuth oxides can be classified into for main groups: (1) modes at frequencies lower than 100 cm^{-1} belong to lattice vibrations originating mostly from Bi–Bi stretching and bending; (2) below 200 cm^{-1}, the Raman Bi–O stretching modes are due to displacements of the bismuth metal-ion; (3) in the 300–600 cm^{-1} spectral region, bridging anion modes are caused mainly by the

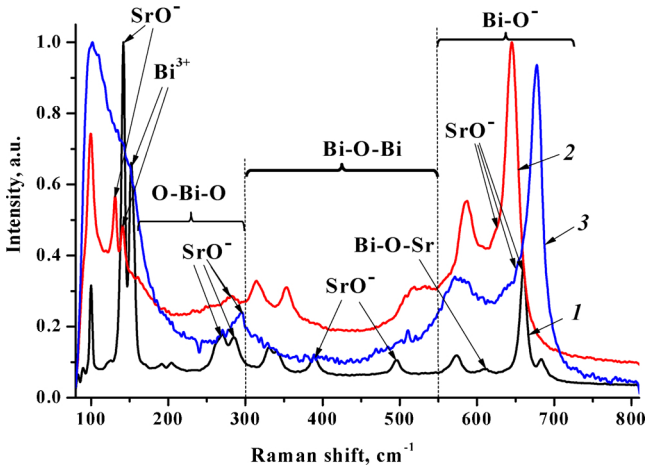

Fig. 4. Raman spectra of synthesized strontium bismuthate samples: (*1*) black spectrum, $Sr_2Bi_2O_5$, (*2*) red spectrum, $Sr_3Bi_2O_6$, and (*3*) blue spectrum, $Sr_6Bi_2O_{11}$.

displacement of the oxygen atom with respect to the Bi atom leading to Bi–O elongation; and (4) Bi–O– non-bridging anion modes occur at 600–700 cm^{-1} [34, 35]. Concurrently, SrO–-related vibrations are present in the 130–140 cm^{-1}, 280–295 cm^{-1}, and 620–660 cm^{-1} spectral region [36–38].

Vibrational modes are more representative and more pronounced in

the Raman spectrum of the $Sr_2Bi_2O_5$ sample (additional bands at 269 cm^{-1}, 390 cm^{-1}, and 496 cm^{-1}); a band at 610 cm^{-1} due to Bi–O–Sr vibrations is also observed. Pertinent band assignments of the main vibrational modes in the Raman spectra are reported in Fig. 4; greater details of the interpretation of Raman data are given in **Table S1**.

Examination of the Raman spectra indicates increased broadening of the peaks in the order: $Sr_2Bi_2O_5 < Sr_3Bi_2O_6 < Sr_6Bi_2O_{11}$, likely due to some structural disorder; oddly, this order parallels the increasing number of oxygen atoms in the bismuthate structures. The stretching anion motion, *i.e.*, the vibrations of bridging oxygens in an angularly constrained Bi–O–Bi configuration (525 cm^{-1}, 300–355 cm^{-1}) destabilizes any structural order. Moreover, increasing the SrO content might convert the BiO_6 units into BiO_3 units thereby producing non-bridging oxygen atoms as observed in some types of binary glasses [39,40]. Indeed, the Bi—O—Bi bridging anion modes in BiO_6 units have practically disappeared in the Raman spectrum of the $Sr_6Bi_2O_{11}$ bismuthate; the Bi–O– non-bridging anion modes in BiO_3 units are the most intense features in the Raman spectrum of Sr_6BiO_{11}. Finally, the presence of BiO_6 octahedral units in $Sr_2Bi_2O_5$ and $Sr_3Bi_2O_6$ indicates that the coordination number of the Sr cations is higher than in the bismuthate $Sr_6Bi_2O_{11}$.

3.3. XPS characterization

The elemental compositions of the surface of the three bismuthates were determined by the XPS method and are reported in **Table S2**, whereas the XPS spectra of the Sr_{3d}, Bi_{4f}, and O_{1s} regions are displayed in Fig. 5.

Analysis reveals the presence of natural carbon contamination on the samples' surface. The C_{1s} peak at 284.8 eV (Fig. 5A) corresponds to the C–C bond, while the peak at ~289 eV suggests CO_2 molecules chemisorbed on the surface of the strontium bismuthates owing to the high affinity of strontium ions for CO_2 molecules. Deconvolution of the Sr_{3d} spectra (Fig. 5B) confirms the presence of surface strontium atoms bound to CO_2 molecules. At the same time, the Bi_{4f} XPS spectra (Fig. 5C) exhibit only one peak that corresponds to the Bi–O bond. Fig. 5D reports the O_{1s} XPS spectra and their deconvolution for all three bismuthates. The O_{1s} peak at ~531.6 eV is associated with the O—C═O bond of chemisorbed CO_2 molecules. Two other peaks at lower binding energies are connected with oxygen atoms in different oxidation states. That is, the peak at 529.5 eV is due to the oxygen dianion O^{2-} in the lattice sites of the bismuthates, while the peak at 530.9 eV is attributed to the interstitial oxygen species O–.

Table 3 summarizes the elemental compositions of the three bismuthates but excludes the contribution of adsorbed CO_2 and makes it possible to determine the stoichiometry of the surface compositions, which are in complete accord with the bulk compositions of the bismuthate samples. For instance, the contribution of interstitial oxygen increases from sample to sample with the SrO content increasing in the order: $Sr_2Bi_2O_5$, $Sr_3Bi_2O_6$, $Sr_6Bi_2O_{11}$ in line with the Raman data that reveal enhanced structural disorder in the same order.

The energies of the uppermost level of the valence band for the three bismuthates were obtained from the lower-energy edges of the XPS spectra (Fig. 6) [41] of the O_{2p} binding energy states (Table 3). These energies vary with the composition of the bismuthate and slightly decrease with increase in SrO content in their cation sublattice. For a discussion on how E_{VB} were estimated based on work functions see the Supplementary Information section.

3.4. Diffuse reflectance (DR) spectroscopy

The as-synthesized bismuthates display different colors (see **Figure S1**) consistent with the increasing absorption of the samples (Fig. 7) in the series $Sr_3Bi_2O_6$ (red spectrum), $Sr_2Bi_2O_5$ (blue spectrum), $Sr_6Bi_2O_{11}$ (black spectrum).

The absorption spectra of the strontium bismuthates in the visible spectral range depend strongly on their chemical composition as manifested in Fig. 7; the absorption edge of the samples red-shifts from $Sr_3Bi_2O_6$ (red spectrum) to $Sr_6Bi_2O_{11}$ (black spectrum). The absorption spectrum of $Sr_2Bi_2O_5$ (Fig. 7) is like the one reported earlier [19,20] in both the position of the absorption band at ca. 2.5 eV (500 nm) and in the features appearing at 3.1–3.6 eV (400–350 nm).

The bandgap energies E_{bg} of the bismuthates (Table 3) were estimated from the DR spectra using the Tauc expression for direct allowed band-to-band optical transitions, modified by substitution of the linear absorption coefficient in the Kubelka-Munk function (Supporting Information, **Figure S7**). Bandgap energy estimates (Table 3) also demonstrate the dependence of the absorption thresholds of the bismuthates on their chemical compositions. The E_{bg} of 3.17 eV for $Sr_2Bi_2O_5$ accords with the bandgap energy (3.2 eV) reported previously [20]. The E_{bg} energies reported in Table 3 were estimated assuming the bismuthates adopt a direct bandgap chosen to compare with recent results reported by Bora and coworkers [1] and by Humayun et al. [4]. If the bismuthates were to adopt indirect bandgaps, estimates (see **Figure S8**) yield E_{bg} = 2.91 eV for $Sr_2Bi_2O_5$, 2.86 eV for $Sr_3Bi_2O_6$, and 1.67 eV for $Sr_6Bi_2O_{11}$. However, the latter indirect bandgap E_{bg} values are inconsistent with the observed color of the samples displayed in **Figure S1**.

3.5. Photocatalytic activity of the bismuthates

3.5.1. Photocatalytic degradation of acetaldehyde in the gas phase

The relative efficiencies of the removal of acetaldehyde in the gas phase are portrayed in Fig. 8, which shows that only the $Sr_6Bi_2O_{11}$ system was able to decompose ca. 0.2 μmol of acetaldehyde during the last 1 hr (out of 2 hrs) of irradiation, while the other two bismuthates had little, if any, effect on the photodegradation, and thus are relatively photoinactive under the conditions used. We hasten to point out that the flow reactor used in the ISO test is such that the photocatalytic reaction occurs only during a single pass of the acetaldehyde to come in contact with the activated photocatalyst surface. Nonetheless, despite this restriction the $Sr_6Bi_2O_{11}$ bismuthate manifested relatively significant photocatalytic activity relative to the other two bismuthates.

3.5.2. Photocatalytic degradation of phenol in aqueous media

Unlike the decomposition of acetaldehyde, the photocatalyzed degradation of phenol in aqueous media was carried out in a batch-type reactor. All samples manifested some degree of photocatalytic activity under otherwise identical experimental conditions (Fig. 9). Expressing photoactivity in terms of reaction rates under the conditions used, the photoactivity of $Sr_6Bi_2O_{11}$ was somewhat greater (k = 1.02 ± 0.11 ppm h^{-1}) than the corresponding photoactivity of Evonik's P25 TiO_2 (k = 0.82 ± 0.09 ppm h^{-1}). The corresponding photoactivities of the other two $Sr_3Bi_2O_6$ and $Sr_2Bi_2O_5$ bismuthates were, respectively, nearly fivefold (k = 0.22 ± 0.06 ppm h^{-1}) and 17-times (k = 0.06 ± 0.05 ppm h^{-1}) smaller. Clearly, $Sr_2Bi_2O_5$ was photocatalytically inactive relative to the $Sr_3Bi_2O_6$ and $Sr_6Bi_2O_{11}$ bismuthates.

That the most efficient bismuthate was $Sr_6Bi_2O_{11}$ in both tests infers that the same or similar mechanistic stages may be implicated in both the gas phase and in aqueous media. To investigate this inference further, we repeated the same experiments for the photodegradation of phenol in aqueous media in the presence of suitably selected radical scavengers.

3.5.3. Photodegradation of phenol in aqueous media in the presence of radical scavengers

The photocatalyzed decomposition of phenol in aqueous media in the presence of the radical scavengers (i) isopranol (IPA), (ii) *p*-benzoquinone (*p*-BQ), and (iii) ammonium oxalate (AO) was carried out to determine the effect(s) of these scavengers on the photocatalytic activity of the strontium bismuthates. To the extent that the bismuthate

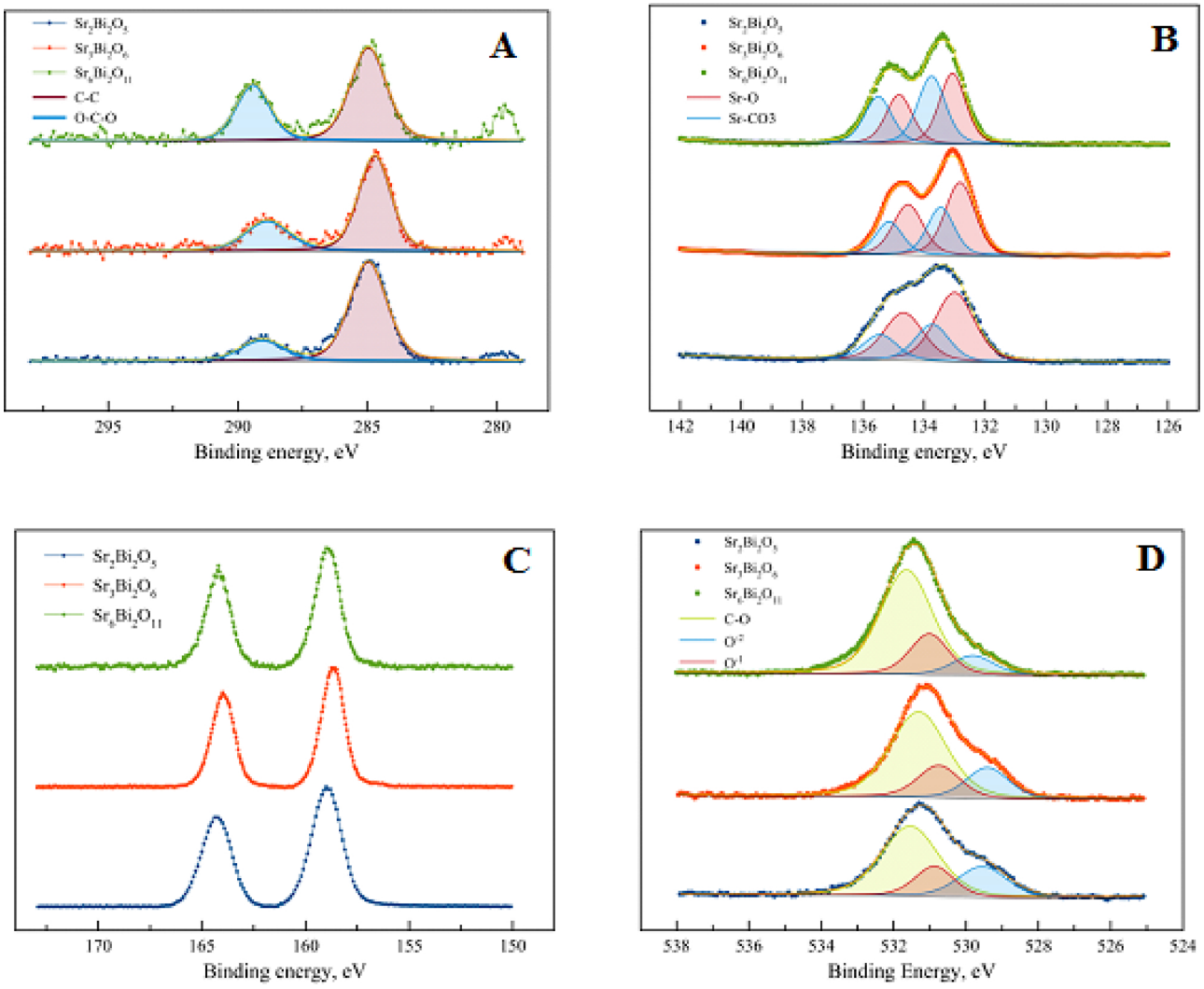

Fig. 5. XPS spectra and the deconvolution results for all synthesized strontium bismuthate samples in C1s (A), Sr3d (B, Bi4f (C), and O1s (D) regions. Spectra are shown in green, red, and blue for $Sr_2Bi_2O_5$, $Sr_3Bi_2O_6$, and $Sr_6Bi_2O_{11}$, respectively.

Table 3
Elemental composition, energies of the upper level in the valence band (E_{VB}) and bandgap energies (E_{bg}) for the three strontium bismuthates.

Properties	$Sr_2Bi_2O_5$	$Sr_3Bi_2O_6$	$Sr_6Bi_2O_{11}$
Element content, (at.%)			
Sr	21.3	26.9	31.6
Bi	23.2	18.4	10.5
O	55.5	54.7	57.9
Including			
O^{2-}	31.0	26.9	20.0
O^-	24.5	27.8	37.9
Sr : Bi : O	2.0 : 2.2 : 5.2	3.0 : 2.1 : 6.1	6.0 : 2.0 : 11.0
E_{VB},[a] (eV)	+1.6	+1.7	+2.2
E_{bg},[b] (eV)	3.17	3.40	2.61

[a] From XPS spectra of the valence band top; energy values are given versus the NHE scale.
[b] Bandgaps from Tauc plots, see text.

[a]From XPS spectra of the valence band top; energy values are given versus the NHE scale.
[b]Bandgaps from Tauc plots, see text.

$Sr_6Bi_2O_{11}$ showed the greatest photoactivity in the removal of acetaldehyde, it was the first bismuthate tested with the radical scavengers (Fig. 10c). Isopropanol showed a slight enhancement of the photoactivity of this bismuthate in the photodegradation of phenol relative to the absence of a "quencher" in the media, and contrary to *p*-

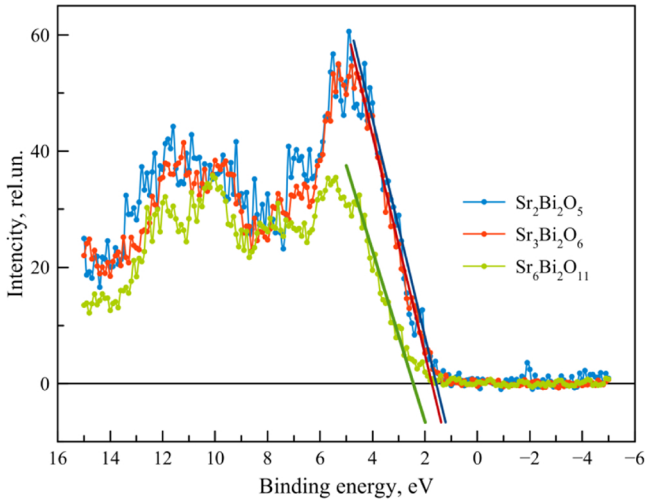

Fig. 6. XPS spectra of the top level of the valence band for the three strontium bismuthate samples. The horizontal black line is the baseline of the XPS signal, whereas the straight lines (blue, red, and green) are the linear extrapolation of the low-energy edge of the XPS spectra of $Sr_2Bi_2O_5$, $Sr_3Bi_2O_6$, and $Sr_6Bi_2O_{11}$, respectively. The binding energy scale is presented relative to the NHE scale in accordance with the methodology presented in ref. [41].

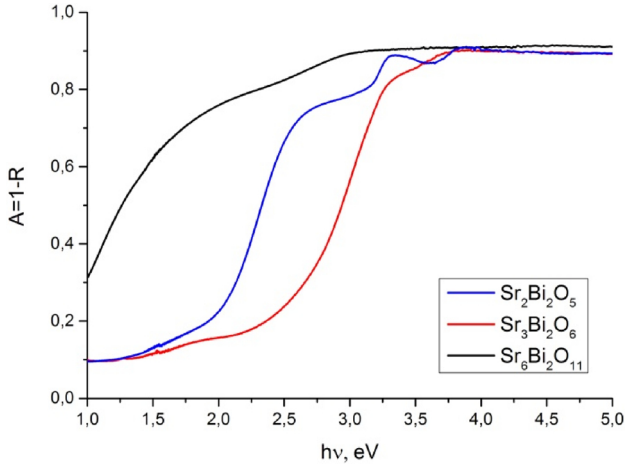

Fig. 7. Diffuse reflectance (DR) spectra displayed as absorption spectra A = 1 – R of the as-synthesized strontium bismuthate samples.

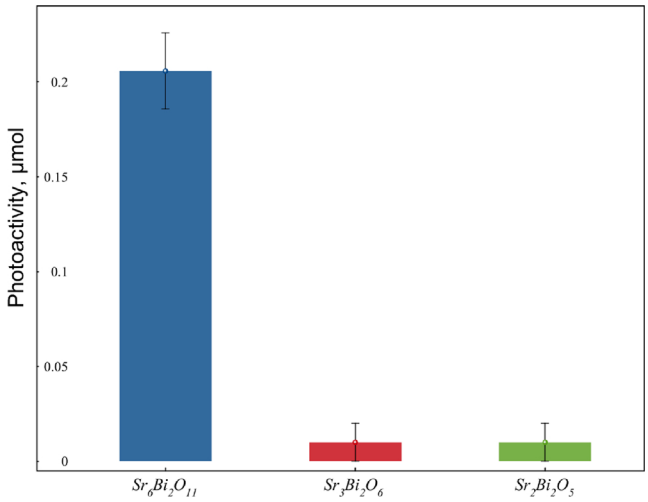

Fig. 8. Photoactivity of the strontium bismuthate samples in the degradation of acetaldehyde in the gaseous phase assessed under otherwise identical conditions (e.g., light source, irradiation times, etc…) and defined by the quantity of substrate decomposed.

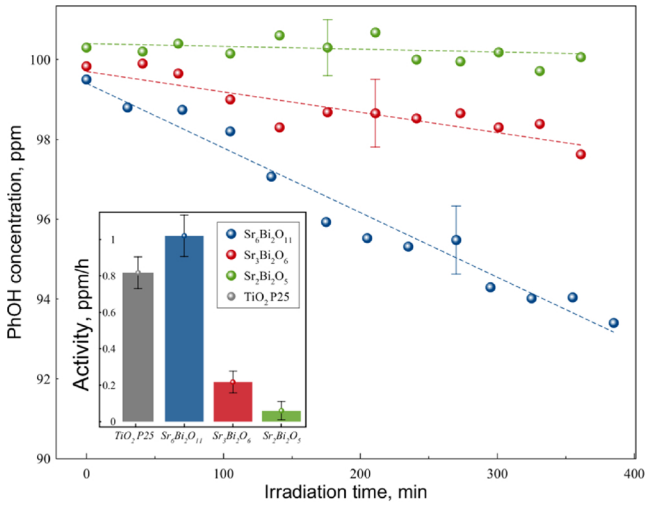

Fig. 9. Changes in the concentration of phenol in aqueous media in the presence of various strontium bismuthate samples. The insert reports the photoactivity as the rate of phenol decomposition by the three strontium bismuthates in comparison with the well-known P25 TiO_2 photocatalyst.

benzoquinone and ammonium oxalate scavengers, which exhibited lower photoactivity of the bismuthate, albeit to different extents. This infers that $Sr_6Bi_2O_{11}$ decomposes phenol via formation of superoxide radical anions on the photocatalyst surface (reductive half-reaction: $O_2 + e^-_{cb} \rightarrow O_2^{-\cdot}$), thereby allowing the free valence band photoholes generated from the activated photocatalyst together with the reactive oxygen species $O_2^{-\cdot}$ to degrade phenol oxidatively. The behavior of the IPA scavenger, well known to scavenge hydroxyl radicals, suggests that the $^{\cdot}OH$ radicals played no role in the phenolic decomposition process involving the $Sr_6Bi_2O_{11}$ bismuthate.

The bismuthate $Sr_3Bi_2O_6$ displayed lower photocatalytic activity in the phenol decomposition process as illustrated in Fig. 10b, which also reveals how the selected radical scavengers affected the phenol decomposition in the presence of $Sr_3Bi_2O_6$. The presence of *p*-benzoquinone and isopropanol had little impact on photoactivity, whereas added ammonium oxalate (scavenger of photoholes) showed significant enhancement (ca. 30 times) of photoactivity of this bismuthate.

The previous test data for the decomposition of acetaldehyde with the bismuthate $Sr_2Bi_2O_5$ showed this ternary oxide to be relatively inactive photocatalytically. Nonetheless, any photocatalytic activity, however small, of this bismuthate might also expose the behavior of the radical scavengers, as occurred with the $Sr_3Bi_2O_6$ sample. Fig. 10a shows that none of the radical scavengers had an effect on the photoactivity of this bismuthate in the phenol decomposition.

3.6. UV-induced coloration of the bismuthate samples

Investigating the photocoloration of metal-oxide photocatalysts might aid our understanding of the events that led up to photocatalyzed processes occurring on the surface of the bismuthate ternary oxides. Two principal stages are involved in the formation of photocatalytic active surface centers: (i) the trapping of photogenerated carriers of a given sign by pre-existing chemically inactive surface defects, and (ii) the subsequent decay of these active states via recombination of a trapped carrier with a free photocarrier of the opposite sign (see: *active state of a surface photocatalytic center* in ref. [42]). Typically, so-called color centers responsible for stable photoinduced coloration of wide bandgap solids are created in the same way in the bulk as they are at the surface of the solid particles. In the latter case, the color centers are the active states of surface photocatalytic centers. Various relationships between the effectiveness of color centers and the formation of photocatalytic centers have been established for a representative set of metal oxides and alkali halides [43,44]. Consequently, the photocoloration of the newly synthesized strontium bismuthates was examined in some detail.

The considerable growth of the absorption bands of the $Sr_2Bi_2O_5$ and $Sr_3Bi_2O_6$ bismuthates in their *extrinsic* absorption region and in the near-fundamental absorption edge from irradiation with UV light (λ = 365 nm, $E_{h\nu}$ = 3.4 eV) under ambient conditions was monitored by diffuse reflectance spectroscopy (Fig. 11a and b). The photoinduced coloration of these two samples was stable and could be annealed noticeably at elevated temperatures (T > 250–400 °C). By contrast, the spectra reported in Fig. 11c for the $Sr_6Bi_2O_{11}$ bismuthate revealed no coloration.

It should be emphasized that the bismuthates $Sr_2Bi_2O_5$ and $Sr_3Bi_2O_6$ that exhibit relatively wide bandgaps (Table 3) and were initially somewhat weakly-colored are photosensitive, while the heavily colored $Sr_6Bi_2O_{11}$ system (**Figure S1**) with the smallest bandgap showed no photocoloration. Similar peculiarities were displayed by the lightly colored (yellow) titania and heavily multi-doped TiO_2 (red and brown) ceramics reported by Kuznetsov and coworkers [45].

UV-induced absorption spectra $\Delta A(h\nu)$ are complex; they consist of the sum of five overlapping Gaussian-shaped single absorption bands for $Sr_2Bi_2O_5$ (Fig. 12a) and three overlapping Gaussian-shaped single absorption bands for $Sr_3Bi_2O_6$ (Fig. 12b). The positions of the absorption maxima (E_m) and half-widths at half-maximum amplitude

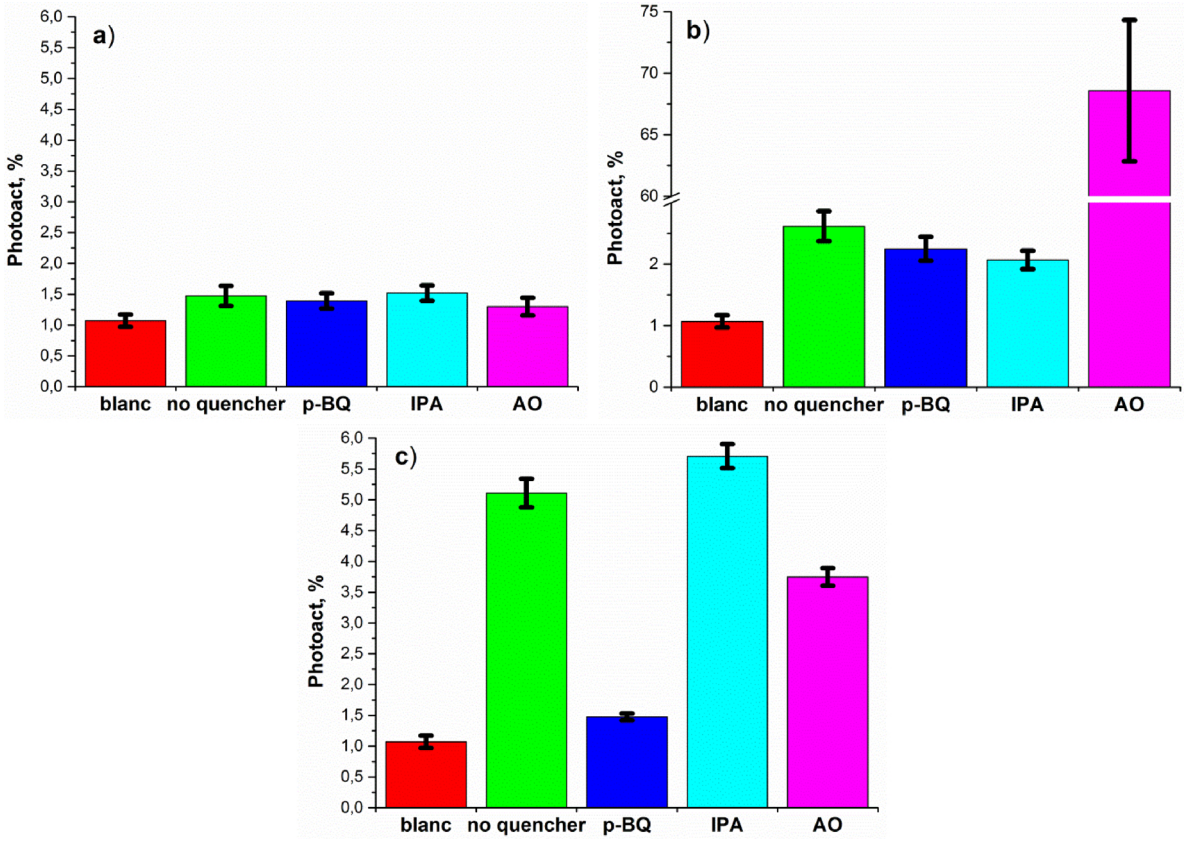

Fig. 10. Phenol concentration changes in aqueous media under irradiation in the presence of selected radical scavengers and strontium bismuthates of various compositions: (a) $Sr_2Bi_2O_5$, (b) $Sr_3Bi_2O_6$, and (c) $Sr_6Bi_2O_{11}$; "blanc" refers to photolysis of phenol with neither the presence of the photocatalyst nor the presence of the selected radical scavengers; "no quencher" signifies only the presence of the photocatalyst in the aqueous media, while p-BQ, IPA, and AO refer to the photodecomposition of phenol in aqueous media in the presence of the photocatalyst and the pertinent scavengers.

(HWHM) are: (i) E_m = 1.08 eV, HWHM = 0.45 ± 0.02 eV; (ii) E_m = 1.91 eV, HWHM = 0.44 ± 0.02 eV; (iii) E_m = 2.14 eV, HWHM = 0.24 ± 0.05 eV; (iv) E_m = 2.88 eV, HWHM = 0.19 ± 0.02 eV; and (v) E_m = 3.11 eV, HWHM = 0.11 ± 0.01 eV for the $Sr_2Bi_2O_5$ system, whereas for the $Sr_3Bi_2O_6$ bismuthate they are (a) E_m = 1.93 eV, HWHM = 0.34 ± 0.05 eV; (b) E_m = 2.43 eV, HWHM = 0.28 ± 0.07 eV; and (c) E_m = 2.83 eV, HWHM = 0.19 ± 0.01 eV. Both the maxima positions of the UV-induced bands (at $E(h\nu) \leq E_g$) and their half-widths (a few tens of eV) are typical of color centers in solids (see, e.g., refs. [43,45,46]).

The UV-induced complex bands of both $Sr_2Bi_2O_5$ and $Sr_3Bi_2O_6$ bismuthates are composed of the sum of a few Gaussian-shaped bands, which originate from different color centers. This assumption is consistent with the kinetic data of the photocoloration of these two bismuthates (Fig. 13); the data were fitted to Eqs. (5).

$$\Delta A(t) = A_1(1 - e^{-t/\tau_1}) + A_2(1 - e^{-t/\tau_2}) \quad (5)$$

where A_1, A_2, τ_1 and τ_2 are constants denoting the ultimate coloration levels (A) and the characteristic coloration times (τ) for the kinetics of coloration of $Sr_2Bi_2O_5$ in the bands at 1.91 eV (***1***) and 2.14 eV (***2***) and of $Sr_3Bi_2O_6$ in the band at 2.42 eV (***3***) under UV irradiation up to 150 min (Fig. 13).

The bi-exponential kinetics Eq. (5) for the UV-induced coloration of powdered Al-doped TiO_2 were reported earlier by Shaitanov and coworkers [46]; the kinetics of coloration were rationalized by a simple model based on a treatment of trapping and detrapping of photogenerated carriers by pre-existing point defects in the solid particles. It should be emphasized that the characteristic times of coloration τ_1 and τ_2, evaluated from Eq. (5), are different for different Gaussian-shaped bands. For instance, τ_1 = 150 ± 40 min and τ_2 = 3.8 ± 1.4 min for the band at 1.91 eV, while τ_1 = 55 ± 10 min and τ_2 = 1.8 ± 0.8 min for the band at 2.14 eV. The same is true for the remaining subbands (Figs. 11a and b and 12). The kinetics of coloration from the sets of Gaussian-shaped subbands, together with some comments regarding the mechanism of UV coloration and bi-exponential kinetics (Eq. (5)) are presented elsewhere (Supporting Information). That discussion suggests that the complex shape of the UV-induced spectra of $Sr_2Bi_2O_5$ and $Sr_3Bi_2O_6$ is due to different color centers rather than to different optical transitions of the same single color centers.

Judging by the maximal amplitudes of ΔA at $E_{h\nu}$ near 2.0 eV for the highly-colored $Sr_2Bi_2O_5$ and $Sr_3Bi_2O_6$ bismuthates (Fig. 11), the effectiveness of photocoloration of $Sr_2Bi_2O_5$ is about threefold greater than for $Sr_3Bi_2O_6$. Likewise, the ultimate level of UV coloration $\{\Delta A(t=\infty) = A_1 + A_2$ (Eqs. (5)$\}$ for the most intense Gaussian-shaped bands are 8.3 ± 2.5% at 1.91 eV ($Sr_2Bi_2O_5$) and 2.16 ± 0.05% at 2.42 eV ($Sr_3Bi_2O_6$) (Fig. 13; see also the discussion on the kinetics of UV coloration of $Sr_2Bi_2O_5$ and $Sr_3Bi_2O_6$ in the Supporting Information, and also Table S3). Thus, on the supposition that the greater is $\Delta A(t=\infty)$ (or ΔA at a fixed irradiation time), the greater is the concentration of induced color centers regardless of the chemical composition of the samples; the order of bismuthates with increasing UV-induced coloration is $Sr_6Bi_2O_{11} < < Sr_3Bi_2O_6 < Sr_2Bi_2O_5$. Interestingly, the photocatalytic activity of the bismuthates in the photodegradation of phenol (Fig. 9) decreases in the order $Sr_6Bi_2O_{11} > Sr_3Bi_2O_6 > Sr_2Bi_2O_5$. If the extent of UV coloration of the bismuthates correlates with their photocatalytic power, it follows that the greater is the efficiency of photocoloration, the lower is the photocatalytic activity of these ternary oxides.

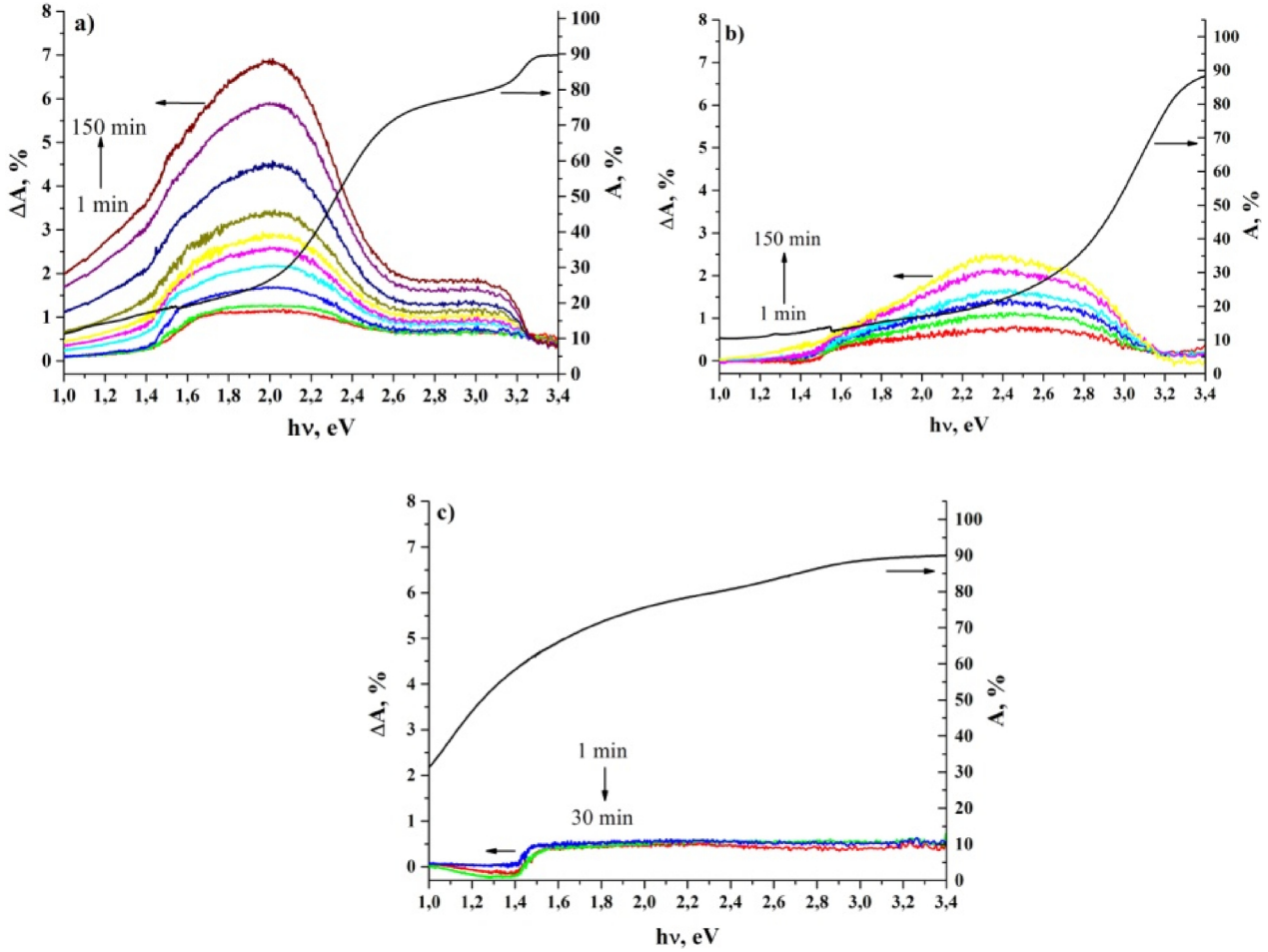

Fig. 11. Difference absorption spectra $\Delta A = A_o - A(t)$ (left ordinate) and absorption spectra $A = 100 - R_o$ (%) (right ordinate) of (a) $Sr_2Bi_2O_5$, (b) $Sr_3Bi_2O_6$, and (c) $Sr_6Bi_2O_{11}$. Here, A_o refers to the absorption of the initial state of the strontium bismuthate samples and A(t) is the absorption of these samples after being irradiated with UV light (λ = 365 nm, irradiance,15 mW cm^{-2}; irradiation time, up to 150 min under ambient conditions in air).

4. Discussion

4.1. Characterization of the bismuthate samples

We noted above that the influence of UV irradiation on strontium bismuthates of a certain composition ($Sr_2Bi_2O_5$ and $Sr_3Bi_2O_6$) results in the formation of absorption bands within the visible spectral region (see Fig. 11). Considering this influence from the point of view of semiconductor band theory, it can be assumed that there exist defective levels within the semiconductor's forbidden bandgap that are filled

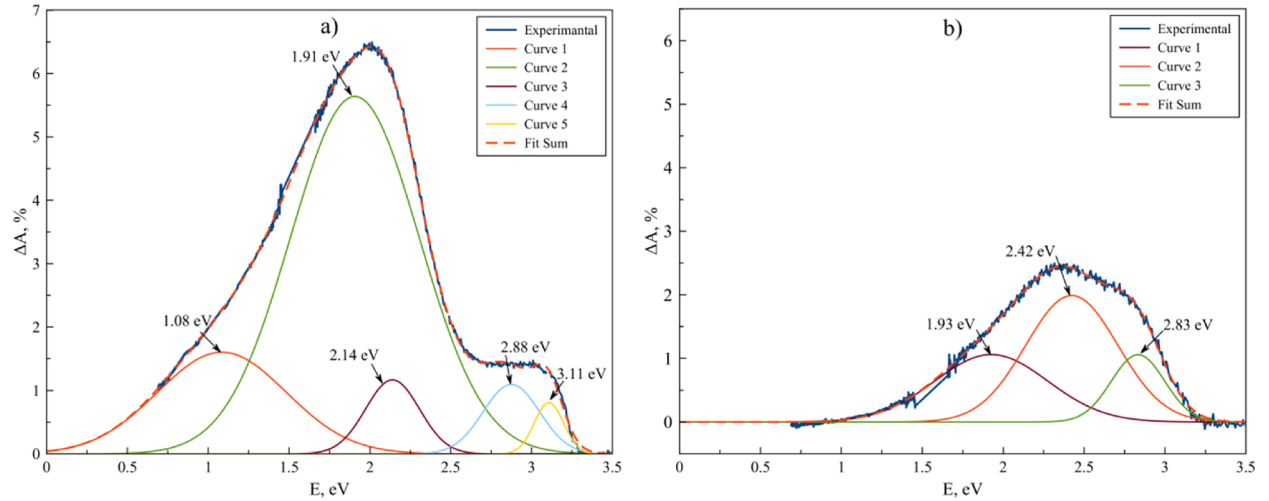

Fig. 12. Difference absorption spectra $\Delta A = A_o$ - A(t) of (a) $Sr_2Bi_2O_5$ and (b) $Sr_3Bi_2O_6$. Here A_o are the absorption of the initial state of the strontium bismuthate samples and A(t) is the absorption of the samples after being irradiated by UV light (λ = 365 nm; irradiance, 15 mW cm^{-2}) for 150 min.

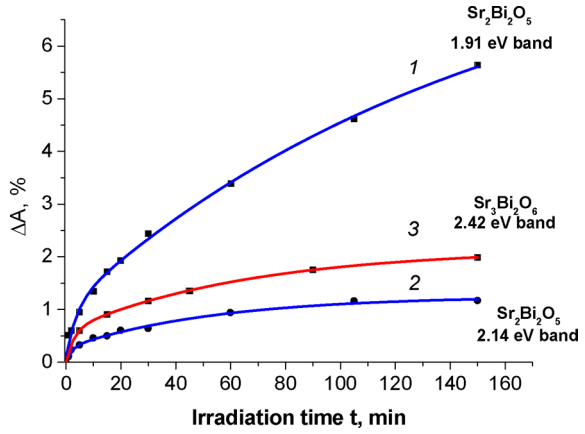

Fig. 13. Kinetics of the UV-induced coloration of $Sr_2Bi_2O_5$ (*1* and *2*, points) and $Sr_3Bi_2O_6$ (*3*, points). The ordinates of the points denote the amplitude of the Gaussian-shaped bands at E(hν) = 1.91 eV and 2.14 eV (*1* and *2*), and at E (hν) = 2.42 eV (*3*) obtained by resolution of the experimental spectra recorded after a set of fixed exposition times (abscissa) into Gaussian bands. The solid lines represent the fittings of the kinetics as per eqn. (5) – see text.

with charge carriers photogenerated under UV exposure.

Crystalline solids always contain native point defects in their lattice formed that form during the synthesis. Some of the most common defects in crystalline solids are the Schottky and the Frenkel defects. A Schottky defect consists of the presence of a vacancy in the crystal lattice; a distinctive feature of such defects is that they are formed in pairs so as to fulfill the condition of neutrality of the crystal lattice. By comparison, a Frenkel defect represents a pair of vacancies and interstitial atoms. Schottky defects are formed more easily in more highly-packed crystal lattices, whereas the Frenkel defects are more likely to form in crystals with large interatomic cavities. The bismuthates examined in the presented study possess relatively large volumes of the unit cell. Consequently, we infer that the basic mechanism of defect formation is likely the Frenkel mechanism.

There also exists an empirical rule according to which atoms of the lightest element will tend to migrate to interstitial positions. In the case of the strontium bismuthates, oxygen is the lightest element so that a large number of anti-Frenkel defects should form such as, for example, “vacancy in the anionic sublattice *plus* an interstitial oxygen”.

The XPS data of Table 3 reveal that all the as-synthesized strontium bismuthates contain a large number of oxygen atoms in the O^- oxidation state. Consequently, we conclude that the oxygen that leaves its normal position in the crystal lattice to form an interstitial oxygen leads to the formation of Frenkel defects.

The equilibrium concentration of Fenkel defects (n) is related to the energy required for moving an atom from its regular lattice site to the interstitial site (ΔE) by the known correlation (eq. (6)):

$$n \approx \sqrt{NN`}\, e^{-\frac{\Delta E}{2kT}} \tag{6}$$

where N and $N`$ denote the concentration of the lattice sites and interstitial positions, respectively; k is Boltzmann's constant, and T is the Kelvin temperature.

If we consider (a) the specific number of oxygen atoms in the O^- state per unit cell of each of the as-synthesized bismuthates to represent the equilibrium concentration of Frenkel defects, (b) the number of atoms in the unit cell of each of the bismuthates to be the concentration of sites, and (c) the number of oxygen atoms in the unit cell of each bismuthate (we assume that Frenkel defects are formed only by small displacements of the oxygen atoms) to denote the concentration of interstitial positions, then it is possible to estimate the energy ΔE for each of bismuthates (Table 4) by transforming Eq. (6) into Eq. (7):

Table 4
Energy of formation of Frenkel defects for the three as-synthesized bismuthates.

Criteria	Sample		
	$Sr_2Bi_2O_5$	$Sr_3Bi_2O_6$	$Sr_6Bi_2O_{11}$
n	2.3	3.1	7.2
N	9	11	19
$N`$	5	6	11
ΔE, meV	55.1	49.4	35.4

$$\Delta E = 2kTln\frac{\sqrt{NN`}}{n} \tag{7}$$

Perusal of Table 4 reveals that the energy of defect formation decreases from 55.1 meV for $Sr_2Bi_2O_5$ to 49.4 meV for $Sr_3Bi_2O_6$ to 35.4 meV for $Sr_6Bi_2O_{11}$ as the number of oxygen atoms in the unit cell increases. It should also be noted that in all the cases considered, the energy of formation of defects of the type described is very small and comparable to the thermal energy. This means that the number of oxygen atoms in the O^- state (“n” in the terminology of Table 4), determined during the experiments, reflects the steady-state dynamic equilibrium between the oxygens and the interstitial states. Thus, formation of defects of this type is not the result of the synthesis method to produce such metal oxides but is determined by the nature of the crystal lattice adopted by each of the as-prepared bismuthates.

UV irradiation of the bismuthates $Sr_2Bi_2O_5$ and $Sr_3Bi_2O_6$ caused the formation of complex absorption bands, which were represented as the sum of several Gaussian-shaped bands (Fig. 11). Also, all the components of these complex absorption bands exhibited saturation-type characteristics (see **Figure S11**). In cases where all the components are saturated, simple calculations yield absorption bands that resemble those illustrated in Fig. 14 for these two bismuthates recalling, however, that formation of such absorption bands was not observed for the other bismuthate $Sr_6Bi_2O_{11}$.

The existence of Frenkel defects suggests that, in the course of photoexcitation, the photoelectron can be captured by an oxygen vacancy with formation of an ***F*** center or by an interstitial oxygen converting such oxygen to the O^{2-} oxidation state. In this case, formation of ***F*** centers is displayed by the formation of absorption bands in the visible spectral region, in contrast to the capture of electrons by interstitial oxygens (see Fig. 15). If this hypothesis reflected the photodegradation processes appropriately, the difference in photocatalytic activity of the various bismuthates in the decomposition of phenol reaction can then be described.

In a typical photocatalytic experiment, 300 mg of a strontium bismuthate sample might be used

to decompose a given substrate (e.g., acetaldehyde, phenol). In that case, taking into account the number of Frenkel defects in a unit cell for each of the as-synthesized bismuthates, it can be shown that the total number of defects in a 300-mg sample would be 6.5×10^{19} for $Sr_2Bi_2O_5$, 6.4×10^{19} for $Sr_3Bi_2O_6$, and 6.1×10^{19} for $Sr_6Bi_2O_{11}$. In addition, in a typical photocatalytic experiment, such as the decomposition of phenol, 300 mL of the aqueous phenolic solution might contain 100 ppm of phenol, in which case the total number of phenol molecules would be 1.0×10^{21}.

The $Sr_2Bi_2O_5$ bismuthate showed relatively no photocatalytic activity. In this case, all the photoelectrons formed during the UV11 irradiation are captured by the oxygen vacancies to form ***F*** color centers that display absorption bands such as those shown in Fig. 14. Simple calculations demonstrate that (in this case) for an absorption band with unit area to appear would necessitate 0.5×10^{19} ***F*** centers. Consequently, the decomposition of phenol in the presence of $Sr_2Bi_2O_5$ will not occur, as demonstrated experimentally, because all the photoelectrons are trapped in oxygen vacancies (Fig. 16).

The bismuthate $Sr_6Bi_2O_{11}$ turned out to be the most active

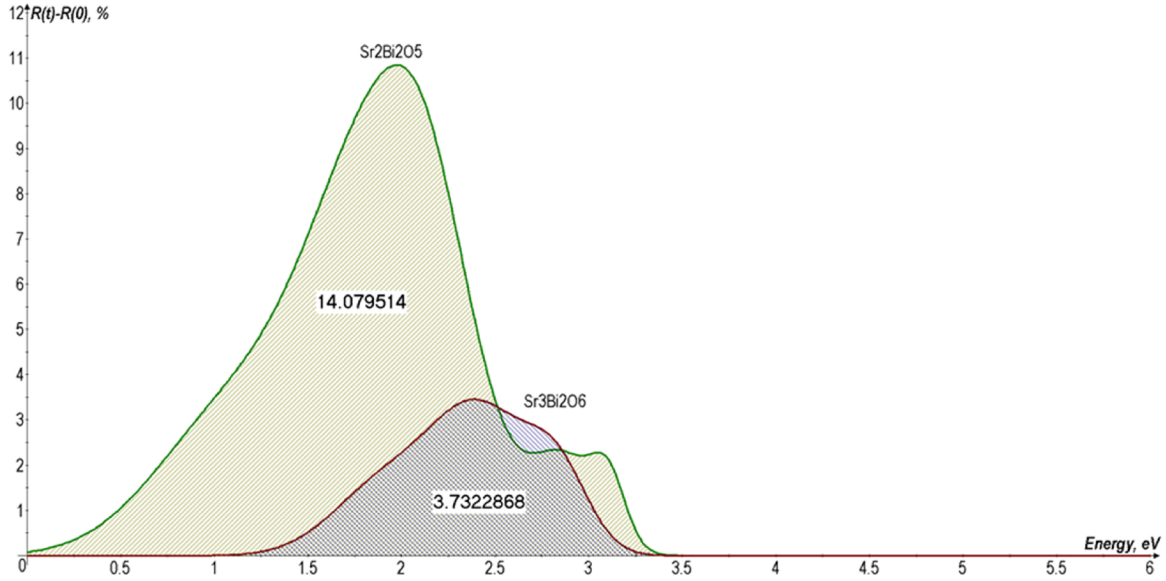

Fig. 14. Results of the simulation of the absorption bands for the $Sr_2Bi_2O_5$ and $Sr_3Bi_2O_6$ bismuthate samples.

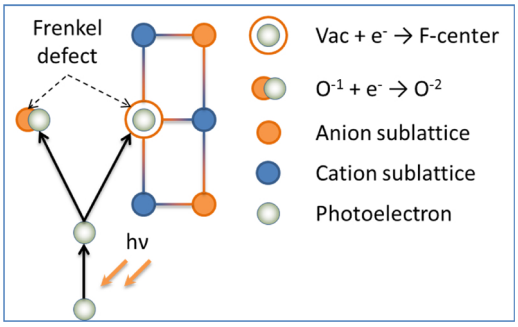

Fig. 15. Scheme depicting a Frenkel defect and its capture of a photogenerated electron; also shown is the capture of an electron by an oxygen vacancy to form an *F* color center.

photocatalyst amongst the three investigated. The rate of decomposition of phenol was 1.02 ppm hr^{-1}, which means that during the 6.5 hrs of the experiment, 6.7×10^{19} molecules of phenol were destroyed. Hence, more than one phenol molecule was destroyed by each point defect during the experiment, indicating that the turnover number was greater than unity (i.e., TON > 1). It would appear then that because of the high photocatalytic activity and the absence of ***F*** centers in such a system, only electrons captured by interstitial oxygens are involved indirectly in the phenol decomposition (Fig. 16).

The $Sr_3Bi_2O_6$ bismuthate occupies an intermediate position between the three bismuthates. On the one hand, an induced absorption band is formed (presumably due to formation of ***F*** centers) as in $Sr_2Bi_2O_5$. On the other hand, $Sr_3Bi_2O_6$ exhibits some photocatalytic activity in the phenol decomposition reaction presumably because photoelectrons are captured by interstitial oxygens as in the $Sr_6Bi_2O_{11}$ case. Thus, electrons can be localized both at interstitial oxygens (and participate in phenol decomposition) and in vacancies with formation of ***F*** centers (Fig. 16).

4.2. Proposed photocatalytic mechanisms

X-ray Photoelectron Spectroscopy (XPS) and Diffuse Reflectance Spectroscopy (DRS) are two spectroscopic methods that afford, respectively, estimates of the energy of the uppermost level of the valence band and the bandgap energies of the strontium bismuthates (Table 3). Also determined were the energy levels of the point defects within the bandgap in the anion sublattice of the bismuthates $Sr_2Bi_2O_5$ and $Sr_3Bi_2O_6$ from the band maxima of the deconvoluted absorption spectra (Fig. 12). Hence, it is possible to construct the band structures of the bismuthates of different compositions (Fig. 17). These structures can infer a scheme to rationalize the photocatalytic processes occurring with each of the bismuthates. The most photoactive of the bismuthates was $Sr_6Bi_2O_{11}$ with a bandgap energy of 2.61 eV, with the energy of the uppermost level in the valence band being +2.22 eV, and the energy of the lowest level in the conduction band being −0.39 eV (versus NHE;

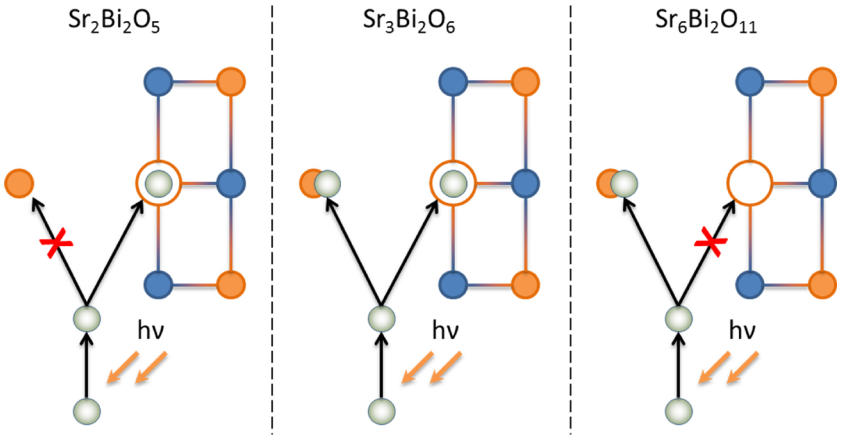

Fig. 16. Possible mechanisms for the capture of photoelectons in the crystal lattice point defects of the three strontium bismuthates; gray balls are the electrons; the lone orange ball denotes an interstitial oxygen, whereas the empty ball refers to an oxygen vacancy. The $Sr_2Bi_2O_5$ bismuthate yields only *F* centers upon capture of electrons by the vacancies; the $Sr_3Bi_2O_6$ sample yields both *F* centers and interstitially captured electrons, whereas in the $Sr_6Bi_2O_{11}$ system electrons are captured by the interstitial oxygens; no *F* centers are formed.

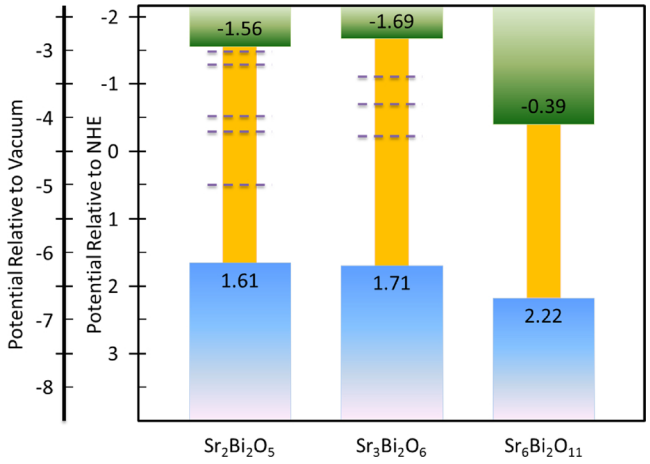

Fig. 17. Band structures of the three strontium bismuthates of various compositions.

Fig. 17).

Let us now consider the processes that take place with the conduction band photoelectrons that will constitute the half-reaction for the oxidative degradation of substrates by the $Sr_6Bi_2O_{11}$ bismuthate. The potential needed to form the superoxide radical anion by electron capture ($O_2 + e^- \rightarrow O_2^{-\cdot}$) is –0.33 eV. Since photoelectrons in the conduction band of $Sr_6Bi_2O_{11}$ turn out to be highly electronegative, formation of the superoxide radical anions $O_2^{-\cdot}$ takes place on the surface of the photocatalyst as attested by the data in experiments involving selected radical scavengers (Fig. 10); the reactive oxygen species $O_2^{-\cdot}$ were the principal active species to impact the photocatalytic activity of $Sr_6Bi_2O_{11}$.

Insofar as processes that involve valence band photoholes and half-reaction components are concerned, the redox potential needed to form $^{\cdot}OH$ radicals by capture of a photohole by surface OH^- ions is +2.27 eV [47] and +2.38 eV for a surficial H_2O molecule. However, these potentials are greater than the energies of the free valence band photoholes so that the reactions $OH^- + h^+ \rightarrow {}^{\cdot}OH$ and $H_2O + h^+ \rightarrow {}^{\cdot}OH + H^+$ are not likely to occur on the surface of the three bismuthates as the flatband potentials of the valence bands are less positive than the above redox potentials (see Figs. 18–21 below). Also, recent studies [48] have shown that the one-electron redox potential of phenol, corresponding to direct transfer of a photohole from the photocatalyst surface to the phenol molecule, is +1.90 eV. From an energy point of view, this is the only process possible as confirmed by the data from experiments with selected radical scavengers (Fig. 10), in which the photoholes are the second most active species to impact the photocatalytic activity of $Sr_6Bi_2O_{11}$.

Fig. 18 illustrates the scheme for the photocatalytic processes involving the bismuthate $Sr_6Bi_2O_{11}$; shown are the $O_2^{-\cdot}$ species that initiate the oxidative decomposition of phenol to its ultimate final products H_2O and CO_2 via the intermediacy of *para*- and *ortho*-benzoquinones. These same intermediates also form during the first stage of the oxidative half-reaction involving the photoholes [49].

The $Sr_3Bi_2O_6$ bismuthate differs significantly from $Sr_6Bi_2O_{11}$ in both composition and energetics. It has a greater bandgap energy (3.4 eV), and the energies of the top of the valence band and the bottom of the conduction band are significantly shifted upward on the NHE scale to +1.71 eV and –1.69 eV, respectively. Let us now entertain the processes that take place with the photogenerated electrons in the $Sr_3Bi_2O_6$ bismuthate. First, an important notable difference in $Sr_3Bi_2O_6$ *vis-à-vis* the $Sr_6Bi_2O_{11}$ system is that during photoactivation by UV light, not only is the conduction band filled with photoelectrons, but the defect levels as well, designated (**1**), (**2**), (**3**) (Fig. 19) and located within the bandgap. These trapped/localized photoelectrons are not involved in further photocatalytic events. As in the previous case, formation of $O_2^{-\cdot}$ species occurs with the participation of conduction band electrons. Based on a suitable arrangement of the levels, the oxidative reaction involving these reactive oxygen species is likely a very significant step toward the ultimate photodegradation of phenol. However, the $Sr_3Bi_2O_6$ system was less photoactive than $Sr_6Bi_2O_{11}$, which leads us to infer that the limiting factor is the channel of the reductive half-reaction involving photoelectrons and oxygen as these photocarriers are trapped by defects within the bandgap.

As evident in the energy scheme of Fig. 19, the oxidative half-reaction cannot occur in any of the mechanisms discussed above, i.e., formation of $^{\cdot}OH$ radicals from oxidation of OH^- ions and/or H_2O, and direct transfer of photoholes to phenol are simply non-players. Therefore, the observed weaker photocatalytic activity of $Sr_3Bi_2O_6$ is most likely caused by a diminished reduction half-reaction, which dampens the rate of phenol decomposition by the superoxide radical anions. Photoholes are known [50] to change the oxidation state of bismuth, in addition to which such a process competes effectively with formation of any $^{\cdot}OH$ radical species as reported by Jiang et al. [51] in similar bismuth oxide structures. Moreover, the oxidative half-reaction in the bismuthates is limited by the number of bismuth species that can be converted from Bi^{III} to Bi^{V}, an occurrence not possible in the bismuthate $Sr_6Bi_2O_{11}$ as bismuth is already in the pentavalent state.

Addition of ammonium oxalate (a scavenger of photoholes) in the degradation of phenol caused a significant increase in the

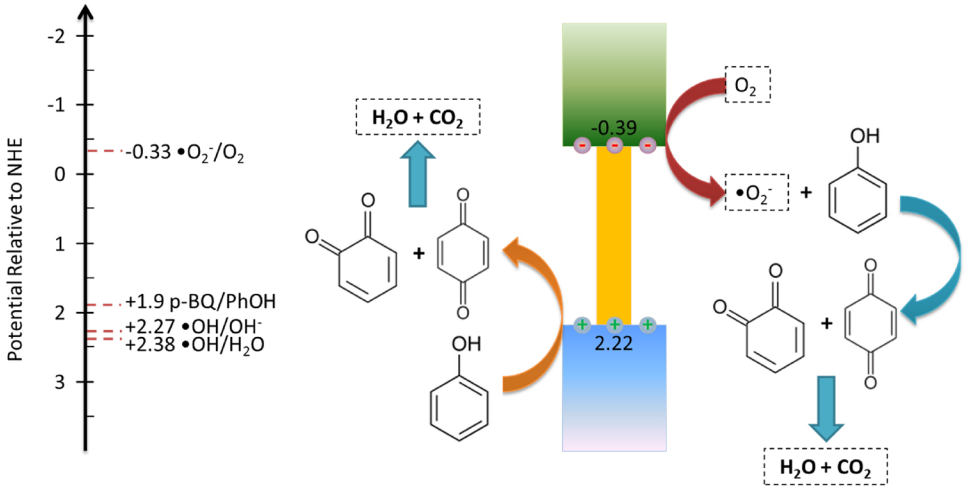

Fig. 18. Scheme illustrating the photocatalytic processes that involve the strontium bismuthate $Sr_6Bi_2O_{11}$.

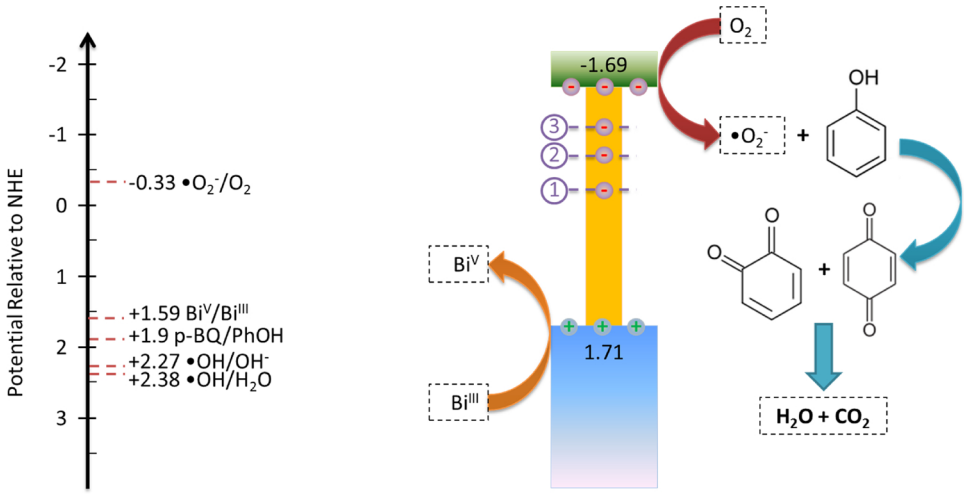

Fig. 19. Scheme depicting the photocatalytic process with the strontium bismuthate $Sr_3Bi_2O_6$.

photocatalytic activity of $Sr_3Bi_2O_6$. An explanation for this observation is found in the mechanistic stages of photostimulated processes depicted in Fig. 20 wherein the oxidative reaction remains the involvement of $O_2^{-\cdot}$ active species. The role of the oxalate scavenger is to eliminate the formed photoholes in the valence band, thereby effectively suppressing electron/hole recombination and enhancing the formation of the $O_2^{-\cdot}$ active species causing the photoactivity to be boosted (Fig. 10b). The direct oxidative decomposition of oxalate by photoholes will be the predominant valence band process rather than $Bi^{III} \rightarrow Bi^{V}$ as the redox potential of the Bi^{V}/Bi^{III} couple is +1.59 eV *versus* +1.15 eV for the oxalate [52].

The bismuthate $Sr_2Bi_2O_5$ displays a similar bandgap energy and relative flatband potentials of the valence and conduction bands with those of $Sr_3Bi_2O_6$: the bandgap energy is 3.17 eV, while the energies of the top of the valence band and the bottom of the conduction band are, respectively, +1.61 eV and −1.56 eV. However, the $Sr_2Bi_2O_5$ sample possesses a larger number of defects (i.e., oxygen vacancies) within the bandgap, which act as very effective electron traps and recombination centers, thereby suppressing the formation of such active species as superoxide radical anions (Fig. 21). This explains the lack of photocatalytic activity of the $Sr_2Bi_2O_5$ bismuthate in the photodegradation of phenol, regardless of whether or not sacrificial electron donors (hole scavengers) are present.

5. Concluding remarks

The present studies examined two novel strontium bismuthate photocatalysts, $Sr_3Bi_2O_6$ and $Sr_6Bi_2O_{11}$, prepared by a solid-state synthesis method; these systems are located in the phase diagram to the right of 50 mol.%, i.e., strontium bismuthates where the number of strontium atoms exceeds the number of bismuth atoms in the cation sublattice. These $Sr_3Bi_2O_6$ and $Sr_6Bi_2O_{11}$ ternary systems, together with $Sr_2Bi_2O_5$ were characterized by various spectroscopic techniques (XRD, XPS, DR, Raman, SEM, EDX and EIS). XPS spectra afforded estimates of the energies of the uppermost level of the valence band and bottommost level of the conduction band; bandgap energies of the bismuthates were determined from DR spectra. Both $Sr_3Bi_2O_6$ and $Sr_6Bi_2O_{11}$ displayed photocatalytic activity toward the photodegradation of acetaldehyde in the gas phase and phenol in aqueous media, with the $Sr_6Bi_2O_{11}$ system exhibiting significantly greater photoactivity vis-a-vis the $Sr_3Bi_2O_6$ bismuthate; by comparison, the bismuthate $Sr_2Bi_2O_5$ proved to be photocatalytically inactive under the experimental conditions used. Detailed mechanisms have been proposed to explain how composition and structure of these three bismuthates affect their photocatalytic activity, aided by examining the UV-induced coloration of all three systems, and by degradation experiments carried out in the presence of suitably chosen radical scavengers. The role of point defects in the crystal lattice (oxygen vacancies) of the bismuthates of differing

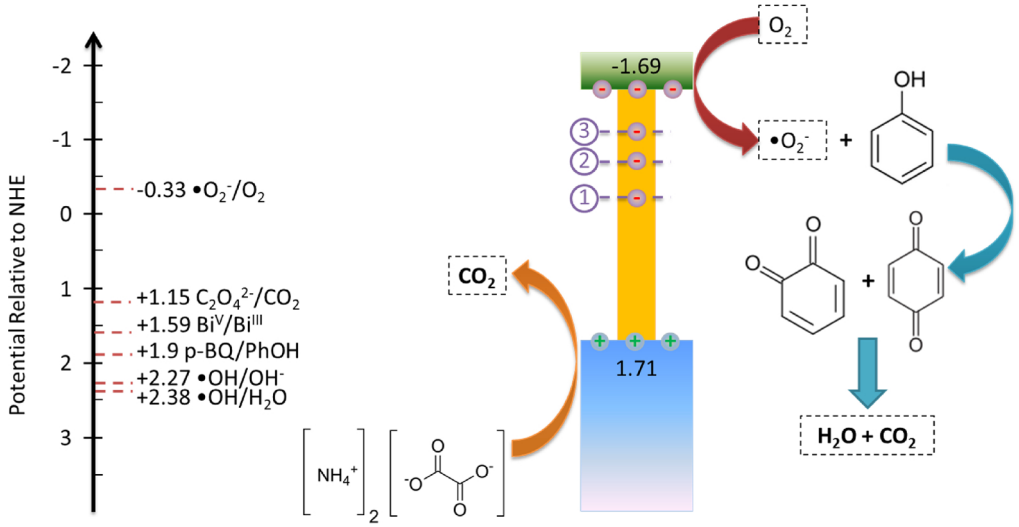

Fig. 20. Scheme illustrating the photocatalytic process involving the strontium bismuthate $Sr_3Bi_2O_6$ and the sacrificial agent ammonium oxalate.

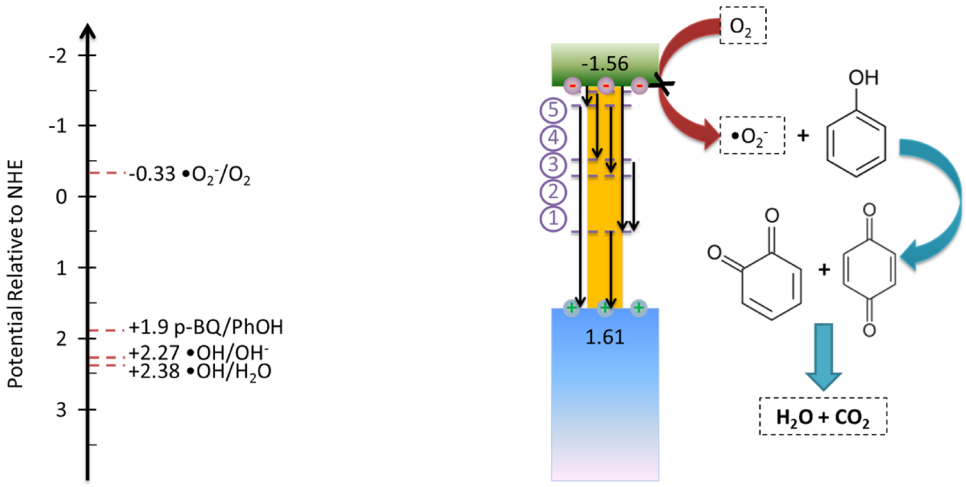

Fig. 21. Flow diagram of the photocatalytic processes involving the strontium bismuthate $Sr_2Bi_2O_5$.

compositions and structures is described for the photodegradation processes as they affect photoactivity by acting as electron traps and as potential recombination centers.

Dedication

This contribution is dedicated to the celebration of the life and scientific contributions of Prof. Ezio Pelizzetti of the University of Torino, Torino, Italy, who was one of the early pioneers of applying photocatalysis to environmental remediation and for his inputs into the understanding of this developing technology until his untimely passing in 2017 after serving as the Rector of that institution for nearly 9 years (2004–2013).

Acknowledgements

The research was kindly funded by a grant from the Russian Science Foundation (project No. 17-73-00007). P.D. Murzin, A.V. Rudakova and V.K. Ryabchuk are grateful for financial support by the Mega-grant (No. 14.Z50.31.0016) from the Government of the Russian Federation within the Project “Establishment of the Laboratory of Photoactive Nanocomposite Materials”. The authors are very grateful to the staff of the Khabarovsk Innovation and Analytical Center of the Yu. A. Kosygin Institute of Tectonics and Geophysics FEB RAS, and the Resource Centers of the Research Park at the Saint-Petersburg State University: (i) Center for Diagnostics of Functional Materials for Medicine, Pharmacology and Nanoelectronics, (ii) Center for Physical Methods of Surface Investigation, (iii) Center for Optical and Laser Materials Research, and (iv) the Nanophotonics Center for their valuable assistance in carrying out the research and in providing the needed equipment. One of us (NS) is grateful to Prof. Angelo Albini for his continued hospitality in the PhotoGreen Laboratory at the University of Pavia, Italy.

References

[1] L.V. Bora, R.K. Mewada, Visible/solar light active photocatalysts for organic effluent treatment: fundamentals, mechanisms and parametric review, Renew. Sustain. Energy Rev 76 (2017) 1393–1421.
[2] X. Wang, F. Wang, Y. Sang, H. Liu, Full-spectrum solar-light-activated photocatalysts for light–chemical energy conversion, Adv. Energy Mater. 7 (2017) 1700473, https://doi.org/10.1002/aenm.201700473 15 pages.
[3] A. Truppi, F. Petronella, T. Placido, M. Striccoli, A. Agostiano, M.-L. Curri, R. Comparelli, Visible-light-active TiO_2-based hybrid nanocatalysts for environmental applications, Catalysts 7 (2017) 100, https://doi.org/10.3390/catal7040100 33 pages.
[4] M. Humayun, F. Raziq, A. Khan, W. Luo, Design of novel visible light active photocatalyst materials: Surface modified TiO_2, Adv. Mater 28 (2016) 5425–5446, https://doi.org/10.1080/17518253.2018.1440324.
[5] K. Qi, B. Cheng, J. Yu, W. Ho, Review on the improvement of the photocatalytic and antibacterial activities of ZnO, J. Alloys Compd. 727 (2017) 792–820.
[6] S. Chen, T. Takata, K. Domen, Particulate photocatalysts for overall water splitting, Nat. Rev. 2 (2017) 17050 17 pages.
[7] A. Lais, M.A. Gondal, M.A. Dastageer, Semiconducting oxide photocatalysts for reduction of CO_2 to methanol, Environ. Chem. Lett. 16 (2018) 183–210, https://doi.org/10.1007/s10311-017-0673-8.
[8] J. Wen, J. Xie, X. Chen, X. Li, A review on g-C_3N_4-based photocatalysts, Appl. Surf. Sci. B 391 (2018) 72–123, https://doi.org/10.1016/j.apsusc.2016.07.030.
[9] X. Li, J. Yu, S. Wageh, A. Al-Ghamdi, J. Xie, Graphene in photocatalysis. A review, Small 12 (2016) 6640–6696.
[10] A. Nikokavoura, Trapalis. Graphene and g-C3N_4 based photocatalysts for NO_x removal: a review, Ch. Appl. Surf. Sci. 430 (2018) 18–52.
[11] R. He, S. Cao, P. Zhou, J. Yu, Recent advances in visible light Bi-based photocatalysts, Chin. J. Catal 35 (2014) 989–1007.
[12] D. Shtarev, V. Ryabchuk, K. Makarevich, A. Shtareva, A. Blokh, I. Astapov, N. Serpone, Calcium bismuthate nanoparticulates with orthorhombic and rhombohedral crystalline lattices: effects of composition and structure on photoactivity, ChemistrySelect 2 (2017) 9851–9863.
[13] Y. Wang, Y. He, T. Li, J. Cai, M. Luo, L. Zhao, Photocatalytic degradation of methylene blue on $CaBi_6O_{10}/Bi_2O_3$ composites under visible light, Chem. Eng. J. 189–190 (2012) 473–481.
[14] Y. Wang, Y. He, T. Li, J. Cai, M. Luo, L. Zhao, Novel $CaBi_6O_{10}$ photocatalyst for methylene blue degradation under visible light irradiation, Catal. Commun 18 (2012) 161–164.
[15] T. Montalvo-Herrera, D. Sanchez-Martinez, L.M. Torres-Martinez, Sonochemical synthesis of CaBi6O_{10} nanoplates: photocatalytic degradation of organic pollutants (ciprofloxacin and methylene blue) and oxidizing species study (h^+, $^{\cdot}OH$, H_2O_2 and $O_2^{\cdot-}$), J. Chem. Technol. Biotechnol 92 (2017) 1496–1502.
[16] Z. Liu, X. Wang, Q. Cai, C. Ma, Z. Tong, $CaBi_6O_{10}$: a novel promising photoanode for photoelectrochemical water oxidation, J. Mater. Chem. A 5 (2017) 8545–8554.
[17] Y.-C. Yang, X. Wang, J. Qu, Preparation and photocatalytic degradation of malachite green by photocatalyst $SrBi_4O_7$ under visible light irradiation, Appl. Mechan. Mater 522–524 (2014) 411–415.
[18] W. Zhou, X. Yu, Use of $Sr_2Bi_2O_5$ as photocatalyst for the degradation of acid red G, Desalin. Water Treat. 30 (2011) 295–299.
[19] Z. Shan, Y. Xia, Y. Yang, H. Ding, F. Huang, Preparation and photocatalytic activity of novel efficient photocatalyst $Sr_2Bi_2O_5$, Mater. Lett. 63 (2009) 75–77.
[20] Y. Obukuro, S. Matsushima, K. Obata, T. Suzuki, M. Arai, E. Asato, Y. Okuyama, N. Matsunaga, G. Sakai, Effects of La doping on structural, optical, electronic properties of $Sr_2Bi_2O_5$ photocatalyst, J. Alloys Compd. 658 (2016) 139–146, https://doi.org/10.1016/j.jallcom.2015.10.199.
[21] X. Hu, C. Hu, J. Qu, Photocatalytic decomposition of acetaldehyde and *Escherichia coli* using NiO/$SrBi_2O_4$ under visible light irradiation, Appl. Catal. B: Environ. 69 (2006) 17–23.
[22] C. Hu, X. Hu, J. Guo, J. Qu, Efficient destruction of pathogenic bacteria with NiO/$SrBi_2O_4$ under visible light irradiation, Environ. Sci. Technol. 40 (2006) 5508–5513.
[23] D.S. Shtarev, A.I. Blokh, E.O. Nashchochin, A.V. Shtareva, The dependence of the conduction band edge of the alkali earth metal bismuthates on their composition, Optic. Quant. Electron. 50 (2018) 228, https://doi.org/10.1007/s11082-018-1498-9.
[24] Hallstedt B, L.J. Gauckler, Revision of the thermodynamic descriptions of the Cu–O, Ag–O, Ag–Cu–O, Bi–Sr–O, Bi–Ca–O, Bi–Cu–O, Sr–Cu–O, Ca–Cu–O and Sr–Ca–Cu–O systems, Comp. Coupling Phase Diagr. Thermochem. 27 (2003) 177–191.
[25] see for example: https://www.malvernpanalytical.com/products/category/software/x-ray-diffraction-software/searchmatch-reference-databases OR http://www.crystalimpact.com/match/download.htm.
[26] NIST X-ray Photoelectron Spectroscopy Database: see http://srdata.nist.gov/.

[27] ISO 22197-2: "Test method for air-purification performance of semiconducting photocatalytic materials, removal of acetaldehyde". See https://shop.bsigroup.com/ProductDetail/?pid=000000000030181337.
[28] D.S. Shtarev, A.V. Shtareva, A.I. Blokh, P.S. Goncharova, K.S. Makarevich, On the question of the optimal concentration of benzoquinone when it is used as a radical scavenger, Appl. Phys. A 123 (2017) 602.
[29] R.S. Roth, C.J. Rawn, B.P. Burton, F. Beech, Phase equilibria and crystal chemistry in portions of the system SrO'CaO-Bi_2Os-CuO, Part II - The System SrO-Bi_2O_3-CuO, J. Res. Natl. Inst. Stand. Technol. 95 (1990) 291–335.
[30] W. Wong-Ng, H.F. McMurdie, B. Paretzkin, M.A. Kuchinski, A.L. Dragoo, Standard X-ray diffraction powder patterns of fourteen ceramic phases, Powder Diffr. 3 (1988) 246–254.
[31] M. Portilla, Oxygen and the formation of new ordered perovskite-based structures in the Bi-Sr-O system, J. Solid State Chem. 105 (1993) 371–377.
[32] R.J. Betsch, W.B. White, Vibrational spectra of bismuth oxide and the sillenite-structure bismuth oxide derivatives, Spectrochim. Acta Part A: Molec. Spectrosc. 34 (1978) 505–514.
[33] S.N. Narang, N.D. Patel, V.B. Kartha, Infrared and Raman spectral studies α-Bi_2O_3, J. Mol. Struct. 327 (1994) 221–235.
[34] R.V. Kumar, A. Edukondalu, B. Srinivas, G. Sriramulu, M.G. Krishna, K.S. Kumar, FTIR and Raman studies on 25Bi2O3-(75-x)B2O3-xBaO glasses, AIP Conference Proceedings 1665 (1995) 070038.
[35] A.A. Kharlamov, R.M. Almeida, J. Heo, Vibrational spectra and structure of heavy metal oxide glasses, J. Non-Cryst. Solids 202 (1996) 233–240.
[36] K.H. Rieder, B.A. Weinstein, M. Cardona, H. Bilz, Measurement and comparative analysis of the second-order Raman spectra of the alkaline-earth oxides with a NaCl structure, Phys. Rev. B 8 (1973) 4780–4786.
[37] C. Gautam, A.K. Yadav, V.K. Mishra, K. Vikram, Synthesis, IR and Raman spectroscopic studies of (Ba,Sr)TiO_3 borosilicate glasses with addition of $La2O_3$, Open J. Inorg. Non-Met. Mater. 2 (2012) 47–54.
[38] A. Dutta, P.K. Mukhopadhyay, T.P. Sinha, S. Shannigrahi, A.K. Himanshu, P. Sen, S.K. Bandyopadhyay, Sr_2SmNbO_6 perovskite: Synthesis, characterization and density functional theory calculations, Mat. Chem. Phys 179 (2016) 55–64.
[39] S. Hazra, S. Mandal, A. Ghosh, Properties of unconventional lithium bismuthate glasses, Phys. Rev. B 56 (1997) 8021–8025.
[40] S. Hazra, A. Ghosh, Structure and properties of nonconventional glasses in the binary bismuth cuprate system, Phys. Rev. B 51 (1995) 851–856.
[41] S.A. Chambers, T. Droubay, T.C. Kaspar, M. Gutowski, M. van Schilfgaarde, Surf. Sci 554 (2004) 81–89.
[42] S.E. Braslavsky, A.M. Braun, A.E. Cassano, A.V. Emeline, M.I. Litter, L. Palmisano, V.N. Parmon, N. Serpone, Glossary of terms used in photocatalysis and radiation catalysis (IUPAC Recommendations 2011, Pure Appl. Chem. 83 (2011) 931–1014.
[43] A.V. Emeline, G.V. Kataeva, V.K. Ryabchuk, N. Serpone, Photostimulated generation of defects and surface reactions on a series of wide band-gap metal-oxide solids, J. Phys. Chem. B 103 (1999) 9190–9199.
[44] V.K. Ryabchuk, Photophysical processes related to photoadsorption and photocatalysis on wide band gap solids: a review, Int. J. Photoenergy 6 (2004) 95–113.
[45] V.N. Kuznetsov, A.V. Emeline, A.V. Rudakova, M.S. Aleksandrov, N.I. Glazkova, V.A. Lovtcius, G.V. Kataeva, R.V. Mikhaylov, V.K. Ryabchuk, N. Serpone, Visible–NIR light absorption of titania thermochemically fabricated from titanium and its alloys; UV- and visible-light-induced photochromism of yellow titania, J. Phys. Chem. C 117 (2013) 25852–25864.
[46] L. Shaitanov, A. Murashkina, A. Rudakova, V. Ryabchuk, A. Emeline, Y. Artemev, G. Kataeva, N. Serpone, UV-induced formation of color centers in dispersed TiO_2 particles: Effect of thermal treatment, metal (Al) doping, and adsorption of molecules, J. Photochem. Photobiol. Sci. 354 (2018) 33–46.
[47] S. Park J. Park, R. Selvaraj, Y. Kim, Facile microwave-assisted synthesis of SnS_2 nanoparticles for visible-light responsive photocatalyst, J. Ind. Eng. Chem 31 (2015) 269–275.
[48] A.S. Pavitt, E. Bylaska, P.G. Tratnyek, Oxidation potentials of phenols and anilines: correlation analysis of electrochemical and theoretical values, Environ. Sci.: Processes Impacts 19 (2017) 339–349, https://doi.org/10.1039/C6EM00694A.
[49] T.A. Enache, A.M. Oliveira-Brett, Phenol and para-substituted phenols electrochemical oxidation pathways, J. Electroanal. Chem 655 (2011) 9–16.
[50] H. Fu, C. Pan, W. Yao, Y. Zhu, Visible-light-induced degradation of rhodamine B by nanosized Bi_2WO_6, J. Phys. Chem. B 109 (2005) 22432–22439.
[51] Y.-R. Jiang, S.-Y. Chou, J.-L. Chang, S.-T. Huang, H.-P. Linand, C.-C. Chen, Hydrothermal synthesis of bismuth oxybromide–bismuth oxyiodide composites with high visible light photocatalytic performance for the degradation of CV and phenol, RSC Adv. 5 (2015) 30851.
[52] B. Sljukic, R. Baron, R.G. Compton, Electrochemical determination of oxalate at pyrolytic graphite electrodes, Electroanalysis 19 (2007) 918–922, https://doi.org/10.1002/elan.200703852.